ELSEVIER

Contents lists available at ScienceDirect

Earth and Planetary Science Letters

journal homepage: www.elsevier.com/locate/epsl



Exhumation and incision of the eastern Central Andes, southern Peru: Low-temperature thermochronology observations



Sarah Falkowski^{a,*}, Todd A. Ehlers^{a,1}, Nadine McQuarrie^b, Chloë O. Glover^b, Nicholas D. Perez^c, Victoria M. Buford Parks^b

- ^a University of Tübingen, Department of Geosciences, Schnarrenbergstr. 94-96, 72076 Tübingen, Germany
- ^b University of Pittsburgh, Department of Geology and Environmental Science, 4107 O'Hara Street, Pittsburgh, PA 15261, USA
- ^c Texas A&M University, Department of Geology and Geophysics, MS 3115, College Station, TX 77843, USA

ARTICLE INFO

Article history:
Received 15 December 2022
Received in revised form 7 May 2023
Accepted 28 June 2023
Available online 30 August 2023
Editor: A. Webb

Dataset link: https://

doi.pangaea.de/10.1594/PANGAEA.955437

Keywords: Central Andes Peru thermochronology climate tectonics erosion

ABSTRACT

Quantifying the impacts of past changes in tectonics or climate on mountain topography has proven challenging. The incision of the eastern Central Andean Plateau has been interpreted as both a result of deformation-related uplift and erosion and climate-driven erosion. Here, we contribute >100 new apatite and zircon (U-Th)/He and fission-track dates from 51 new and eight previous bedrock samples. These samples were combined with previous thermochronometer data from three \sim 190-km-long and \sim 200-km-apart across-strike transects along the eastern margin of the Andean Plateau in southern Peru. We discuss age-distance, age-elevation, and inverse thermal history model results along these transects to constrain the timing and extent of recent canyon incision compared to the region's long-term (~40 Myrs) exhumation history. Results indicate that, along the plateau flank, long-term, deformation-related exhumation is superimposed by a regional, synchronous canyon incision-related signal since \sim 4-3 Ma. This incision is traceable from at least the Abancay Deflection in southern Peru to southern Bolivia along the eastern Central Andes. Based on the regional and synchronous character of canyon incision across areas with different deformation histories and exhumation magnitude, we suggest that paleoclimate change was a significant contributor to incision. However, structural processes resulting in surface uplift, erosion, and exhumation continued post-mid Miocene and contributed to the observed exhumation magnitude.

© 2023 The Author(s). Published by Elsevier B.V. This is an open access article under the CC BY-NC license (http://creativecommons.org/licenses/by-nc/4.0/).

1. Introduction

The spatio-temporal evolution of mountain topography, including that of orogenic plateaus, is often discussed in terms of two endmembers exerting the largest influence, tectonics and geologic setting vs. climate-driven surface processes (e.g., Montgomery et al., 2001; Kirby et al., 2003; Lamb and Davis, 2003; Bookhagen and Strecker, 2012; Ferrier et al., 2013; Lease and Ehlers, 2013; Gasparini and Whipple, 2014; Godard et al., 2014; Eude et al., 2015). However, quantifying the impacts of past changes in tectonics or climate on the landscape has proven challenging. Incision of the

E-mail addresses: sarah.falkowski@uni-tuebingen.de (S. Falkowski), todd.ehlers@glasgow.ac.uk (T.A. Ehlers), nmcq@pitt.edu (N. McQuarrie), chloe.glover@pitt.edu (C.O. Glover), ndperez@tamu.edu (N.D. Perez), vmbparks@gmail.com (V.M. Buford Parks).

eastern Central Andean Plateau has been interpreted as both a response to deformation-related rock and surface uplift and erosion, and climate-driven erosion (e.g., Kennan et al., 1997; Jeffery et al., 2013; Lease and Ehlers, 2013; Whipple and Gasparini, 2014; Gérard et al., 2021a,b), placing it in the center of the debate between these endmember processes.

For the eastern plateau margin, Lease and Ehlers (2013) suggested that regional canyon incision occurred since 4–3 Ma and was triggered by paleoclimate change that resulted in enhanced precipitation and erosion, in the absence of deformation. This interpretation was based on thermochronometer exhumation data from southeastern Peru (San Gabán Canyon; Fig. 1) and correlations with regional geologic observations and paleoclimate. In contrast, for northern Bolivia and, by implicit extension, southern Peru, Whipple and Gasparini (2014) analyzed different topographic metrics and available denudation rate estimates and found limited evidence for climate-driven erosion. They suggested that recent uplift concentrated incision above deep basement structures. In other studies, Gérard et al. (2021a,b) suggested climate-enhanced inci-

^{*} Corresponding author.

 $^{^{1}}$ Now at University of Glasgow, School of Geographical and Earth Sciences, Glasgow, G12 8QQ, UK.

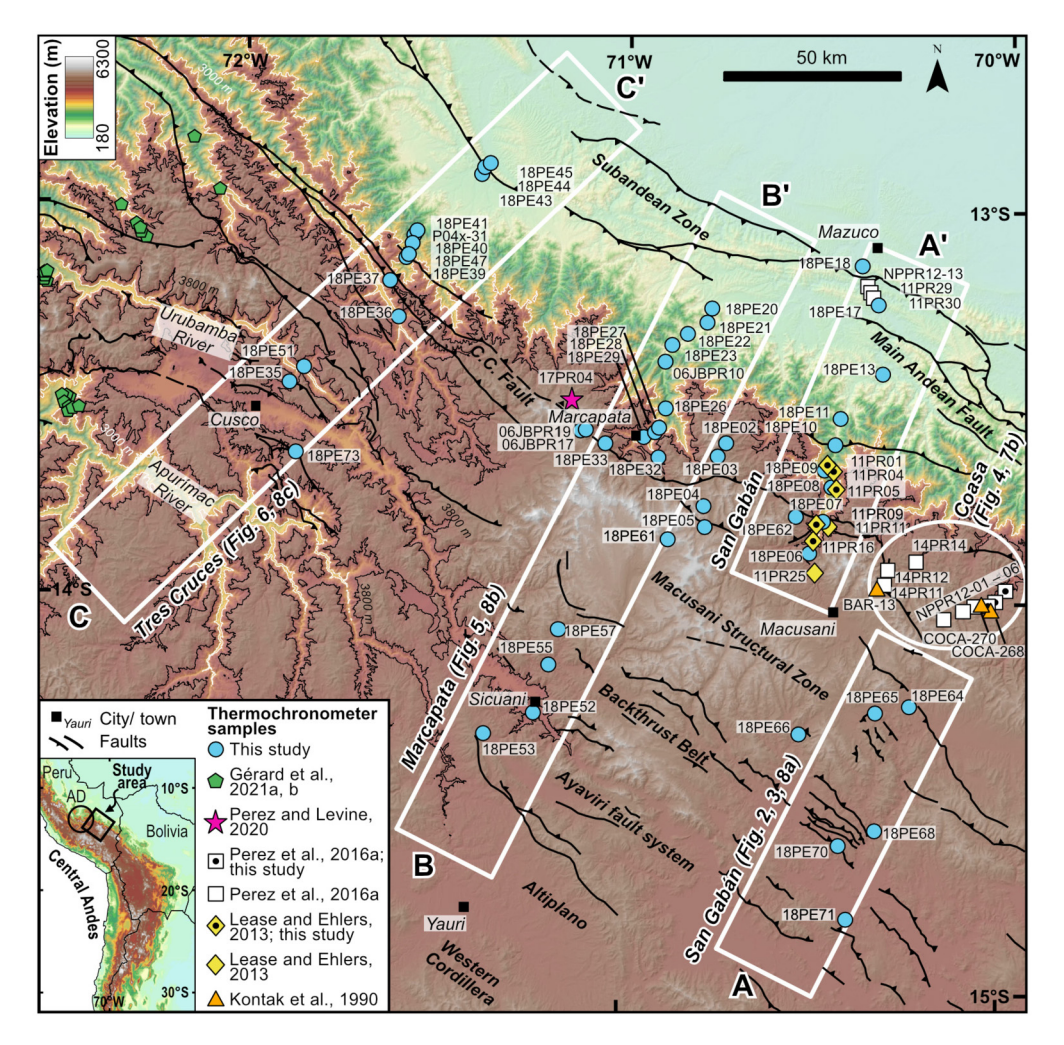


Fig. 1. Topography of the study area in the eastern Central Andes in southern Peru (based on a 90-m-digital elevation model). The map shows new and previous bedrock sample locations for AHe, AFT, ZHe, and ZFT data. Fault lines (simplified from Perez et al., 2016a; INGEMMET, 2022) and major tectonomorphic zones are indicated. The white boxes mark sample transects and topographic swath profiles A-A' (San Gabán), B-B' (Marcapata), and C-C' (Tres Cruces). The white ellipse marks the Permo-Triassic Coasa Pluton area. Abbreviations include AD for the Abancay Deflection (circle in the inset map) and C.C. Fault for the Cordillera de Carabaya Fault.

sion in combination with tectonic uplift driven by out-of-sequence backthrust faulting for the Abancay Deflection area (Fig. 1), where they also observed an increase in the exhumation rate at 4 Ma. However, the mechanisms invoked are not well constrained and studies on the deformation and exhumation across the eastern plateau margin in southern Peru are rare and restricted in space (Kontak et al., 1990; Ruiz et al., 2009; Gotberg et al., 2010; Lease and Ehlers, 2013: Perez et al., 2016a; Baby et al., 2018; Perez and Levine, 2020; Gérard et al., 2021a,b).

Additional observations are needed to constrain the temporal and spatial pattern of canyon incision and long-term deformation and exhumation across the eastern margin of the Peruvian Andes. These observations are needed to evaluate possible tectonic vs. climate change mechanisms associated with topographic development. The focus of this study is to provide these observations from thermochronology data. More specifically, we present new apatite and zircon (U-Th)/He (AHe and ZHe) and apatite and zircon fission-track (AFT and ZFT) data from 51 new and eight previous bedrock samples from three, up to 190-km-long and 200-km-apart across-strike transects (San Gabán, Marcapata, Tres Cruces; Fig. 1). These data are combined with published data and used to conduct inverse thermal history modeling to identify spatial and temporal variations in rock cooling due to exhumation. The transects extend from the eastern Andean Plateau across the Eastern Cordillera to the Subandean foreland and include plateau, interfluve, and canyon bottom samples. This thermochronometer sampling approach allows for the evaluation of age-elevation and age-distance relationships that can be integrated with thermo-kinematic modeling of structural cross-sections. In related studies, we do this integration for the San Gabán and Marcapata regions (see Buford Parks et al., 2023, and Glover et al., 2023) to quantify the deformation history and evaluate the role of deformation, uplift, and canyon incision on the measured thermochronometer data.

2. Background

2.1. Tectonic and geologic background

Cenozoic crustal thickening associated with the subduction of the Nazca Plate beneath western South America formed the Central Andes (e.g., Isacks, 1988). In southern Peru, the Central Andes comprise the forearc, the Western Cordillera (present-day location of the volcanic arc), the northern Altiplano (an internally drained syn-orogenic basin), the Eastern Cordillera (bivergent, thick-skinned segment of the retroarc fold-and-thrust belt, composed of Paleozoic–Mesozoic marine and non-marine strata), and the Subandean Zone (actively deforming thin-skinned segment of the fold-and-thrust belt, composed of Mesozoic–Cenozoic strata) (e.g., Isacks, 1988; Allmendinger et al., 1997; Horton et al., 2002). The Central Andean Plateau is defined as a low-relief, >3 km

elevation region that comprises the Altiplano and parts of the Western and Eastern cordilleras (Isacks, 1988; Allmendinger et al., 1997). The Eastern Cordillera, structurally bound by the Ayaviri and Main Andean fault systems (e.g., Carlotto, 2013; Perez and Horton, 2014), comprises the largest part of the study area (Fig. 1, Fig. S1). The Eastern Cordillera is subdivided into three zones with northeastward stepwise increasing structural elevations, including: (i) a backthrust belt containing southwest-verging thrusts that expose mostly Cretaceous strata (McQuarrie and DeCelles, 2001), (ii) a zone that exposes Devonian to Permian strata and includes in the San Gabán area the Macusani Structural Zone composed of Permo-Triassic syn-rift volcaniclastics and thrust-related reactivation of rift structures (Perez et al., 2016a,b), and (iii) a northeastern segment exposing Ordovician-Devonian strata and Permo-Triassic intrusives that encompass the high-relief plateau flanks and lowerrelief portions toward the Subandes. Deformation of the Eastern Cordillera began 55-40 Ma and migrated northeastward to the Subandes after 20 Ma (e.g., Farrar et al., 1988; Barnes et al., 2008; Perez and Levine, 2020).

2.2. Thermochronology background

Thermochronology is commonly used to reconstruct the exhumation history of upper crustal rocks. In fold-and-thrust belts, thermochronometric ages can represent cooling related to (i) erosional exhumation associated with deformation (e.g., vertical motion of stratigraphy up a structural ramp) that results in the development of topographic relief upon which surface processes act (e.g., McQuarrie and Ehlers, 2017), (ii) erosional exhumation associated with changes in climate-driven surface processes, or (iii) thermal relaxation after magmatic activity. The latter is not an issue in the study area, where intrusions are mostly of Permo-Triassic age (Lancelot et al., 1978; Kontak et al., 1990; Mišković et al., 2009; Perez and Levine, 2020) and samples were collected distal from Cenozoic volcanics (Fig. S1).

Previous exhumation studies in the eastern Peruvian Andes mainly reflect Eocene–Pleistocene rock cooling (e.g., Kontak et al., 1990; Lease and Ehlers, 2013; Perez et al., 2016a; Perez and Levine, 2020; Gérard et al., 2021a,b). This interpretation comes from AHe, AFT, and ZHe thermochronometers that have nominal closure temperatures of \sim 68 °C (Farley, 2000), \sim 110 °C (Ketcham et al., 2007), and \sim 180 °C (Reiners et al., 2004), respectively. To the southeast of the study area, minimum $^{40}{\rm Ar}/^{39}{\rm Ar}$ and K-Ar dates (closure temperatures of \sim 300 °C and higher, e.g., Harrison et al., 1985) are \sim 37 Ma (Farrar et al., 1988; Kontak et al., 1990). Along our sample transects, however, available $^{40}{\rm Ar}/^{39}{\rm Ar}$ data reflect Cretaceous and older rock cooling (Kontak et al., 1990). Based on the previous studies, we targeted the collection of new AHe, AFT, ZHe, and ZFT (nominal closure temperature of \sim 240 °C; e.g., Brandon et al., 1998) thermochronometry to identify the long-term and most recent exhumation.

The notion of reset thermochronometric ages applied in our analysis refers to samples that resided above closure temperatures required to reset ages (e.g., following burial by sediments or thrust sheets). In contrast, partially reset ages reflect the heating of rocks to temperatures close to the closure temperature. Depending on the individual grains' kinetics, single grains will show a range of ages younger and older than the reheating phase. Unreset ages indicate that post-depositional reheating of a sample never reached thermochronometer closure temperatures.

3. Samples and methods

3.1. Samples

We collected a total of 51 new bedrock samples along three across-strike transects reaching from the Andean Plateau to the

Subandes (Fig. 1, Table 1). For the San Gabán transect, we combined 16 new and ten previous samples. For five of those previous samples, we added a total of seven new AFT and ZFT analyses (Fig. 1, Table 2). In addition, 12 previous samples exist from the Permo-Triassic Coasa Pluton area, which is located where our San Gabán transect has a lateral offset (ellipse in Figs. 1, S1). We analyzed three of those samples with the AFT technique (Fig. 1, Table 2). For the Marcapata transect, we combined 22 new and one existing sample. Finally, for the Tres Cruces transect, we collected 13 new samples (Fig. 1, Table 2).

Sample lithologies are granitoids, metasediments, and clastic and volcaniclastic sediments with emplacement and depositional ages that are mostly Cretaceous and older (Table 1, Fig. S1). One sedimentary bedrock sample from the Subandes has an Oligocene–Miocene depositional age (18PE18; Table 1).

3.2. Apatite and zircon (U-Th)/He thermochronology

Apatite and zircon concentrates were obtained from standard mineral separation techniques. Picking criteria for single-grain analysis included crystal transparency to attest to the absence (or minuscule presence) of visible inclusions, the absence of fractures and broken parts, and grain diameters of >60 µm (e.g., Reiners, 2005). If sufficient suitable grains were available, we selected four apatites and four zircons per sample for whole-grain helium, uranium, and thorium (and samarium for apatites) measurements via isotope dilution mass spectrometry. Analytical procedures followed the protocol outlined by Stübner et al. (2016), except for grain mass determination and alpha-ejection correction, which followed the approach of Glotzbach et al. (2019). All analyses were conducted at the University of Tübingen. We calculated weighted mean ages with weighted mean standard deviations (1 σ) for reset samples. For consistency of data presentation, and in light of new data from some of the previous samples, we re-evaluated and recalculated previous (U-Th)/He ages when possible.

3.3. Apatite and zircon fission-track thermochronology

We conducted AFT and ZFT dating using the external detector and zeta-calibration techniques (Hurford, 1990) at the University of Tübingen. Apatites and zircons were mounted in epoxy resin and Teflon, respectively, ground, polished, and etched. Apatites were etched at 21 °C for 20 s in 5.5 M HNO3, and zircons were etched in a KOH:NaOH melt at 228 °C for 18–45 h (Hurford, 1990; Garver, 2003; Donelick, 2005). Sample and age standard mounts and dosimeter glasses (IRMM540, IRMM541) were covered with mica detectors and irradiated at the nuclear reactors in Garching, Germany (apatites), and Mol, Belgium (zircons). Following this, micas were etched in ${\sim}40\%$ -HF for 30 min. Fission tracks and D_{par} (for apatites) were counted and measured at 1000X magnification. The grains did not contain sufficient confined tracks for length measurements. We report fission-track central ages with 1σ -error.

3.4. Inverse thermal history modeling

Inverse thermal history modeling was conducted using the QTQt software (version 5.8.0), which applies a Bayesian transdimensional Markov chain Monte Carlo inversion scheme (Gallagher, 2012). We performed modeling for reset samples with multiple thermochronometers available to investigate rock cooling resulting from exhumation. Therefore, we set no model constraints that describe the samples' emplacement or depositional age. The oldest thermochronometer age of each sample defined the time-temperature space to search for viable thermal models. The present-day temperature was set at $15\pm10\,^{\circ}\text{C}$. Reheating was not allowed. For each thermal history, we ran at least 100,000 burn-in

Table 1 Coordinates, lithologies, and formation ages of new and previous bedrock samples used in this study.

ample	Elevation (m)	Latitude	Longitude	Lithology	Formation age
8PE02	4537	-13.60133	-70.73628	granite	Permian-Triassic
8PE03	4337	-13.63714	-70.75989	granite	Permian-Triassic
8PE04	4731	-13.76361	-70.79339	granite	Permian-Triassic
8PE05	4524	-13.81742	-70.79008	volcaniclastic sediment	Permian-Triassic
8PE06	3791	-13.88008	-70.51325	volcaniclastic sediment	Permian-Triassic
8PE07	2775	-13.80531	-70.47706	granite	Lower Jurassic
8PE08	2030	-13.71064	-70.45511	granite	Permian-Triassic
8PE09	1756	-13.66758	-70.47750	granite	Permian-Triassic
8PE10	1134	-13.60211	-70.45044	quartzite	Ordovician
8PE11	858	-13.53333	-70.43631	slate	Ordovician
8PE13	484	-13.41850	-70.32911	quartzite	Ordovician
8PE17	407	-13.24342	-70.34292	sandstone	Upper Cretaceous
8PE18	359	-13.14269	-70,38858	sandstone	Oligocene-Miocene
8PE20	709	-13.25836	-70.77969	quartzite	Neoproterozoic
8PE21	754	-13.29494	-70.79214	granite	Neoproterozoic
SPE22	851	-13.32394	-70.84208	metasediment	Neoproterozoic
3PE23	959	-13.35333	-70.88253	granite	Devonian
8PE26	1935	-13.51667	-70.89689		Permian-Triassic
				granite	
SPE27	2289	-13.56497	-70.91533	granite 	Permian-Triassic
SPE28	2416	-13.57769	-70.92556	granite	Permian-Triassic
3PE29	2603	-13.59019	-70.95283	granodiorite	Permian-Triassic
8PE32	3367	-13.64156	-70.91547	granite	Permian-Triassic
BPE33	3988	-13.60606	-71.05292	slate	Ordovician
3PE35	3772	-13.46061	-71.88436	sandstone	Permian-Triassic
3PE36	2920	-13.29069	-71.60069	slate	Silurian-Devonian
3PE37	3490	-13.19803	-71.62300	slate	Ordovician
3PE39	2176	-13.12994	-71.57667	fine quartzite in slate	Ordovician
3PE40	1828	-13.07642	-71.55689	granite	Permian-Triassic
8PE41	1420	-13.05431	-71.54208	diorite	Ordovician
8PE43	655	-12.92422	-71.38644	granite	Permian-Triassic
3PE44	540	-12.90492	-71.37589	quartzite	Devonian
3PE45	588	-12.89850	-71.36939	quartzite	Carboniferous
3PE47	1924	-13.10072	-71.56517	quartzite	Permian-Triassic
3PE51	2993	-13.42072	-71.84608	volcaniclastic sediment	Permian-Triassic
8PE52	3605	-14.30000	-71.23147	quartzite	Devonian
3PE53	4138	-14.35300	-71.36247	quartzite	Upper Cretaceous
3PE55	3963	-14.17569	-71.19392	quartzite	Upper Cretaceous
8PE57	4251	-14.08567	-71.16922	quartzite	Lower Cretaceous
8PE61	5042	-13.85064	-70.88708	volcanic	Permian-Triassic
3PE62	4373	-13.78664	-70.55150	granite	Permian-Triassic
8PE64	4185	-14.26847	-70.24386	volcaniclastic sediment	Permian-Triassic
3PE65	4222	-14.28458	-70.33411	volcanic	Permian-Triassic
8PE66	4285	-14.34333	-70.53350	volcaniclastic sediment	Permian-Triassic
8PE68	3954	-14.58686	-70.32919	volcanic	Permian-Triassic
3PE70	4017	-14.62694	-70,42353	volcanic	Permian-Triassic
SPE71	3939	-14.81522	-70.40100	quartzite	Upper Jurassic-Lower Cretace
3PE73	4096	-13.63939	-71.86622	quartzite	Cretaceous?
SJBPR10	1097	-13.39673	-70.89998	meta-granite	Neoproterozoic
SJBPR17	3971	-13.57251	-71.10477	granite	Permian-Triassic
SIBPR19	4269	-13.57440	-71.12007	granite	Permian-Triassic
9			-71.55656	•	
)4x-31	1750	-13.07149	-/1.55656	granodiorite	Permian-Triassic
IPRO1 ^a	1562	-13.64980	-70,47370	diorite-granitoid	Permian-Triassic
IPR04 ^a	1759	-13.66740	-70.47760	granodiorite	Permian-Triassic
IPRO5 ^a	2056	-13.71060	-70.47760 -70.45540	granodiorite	Permian-Triassic
PR09 ^a	2775	-13.80720	-70.47940 -70.47520	plutonic	Lower Jurassic
PR11 ^a	2974	-13.80830	-70.47520	plutonic	Lower Jurassic
PR16 ^a	3240	-13.84660	-70.50430	plutonic	Lower Jurassic?
PR25 ^a	4161	-13.92850	-70.49860	sandstone	Permian-Triassic
PPR12-01 ^b	3950	-13.96729	-69.99659	plutonic	Permian-Triassic
PPR12-02 ^b	3710	-13.99442	-70.02020	plutonic	Permian-Triassic
PPR12-03 ^b	3802	-14.00792	-70.04401	plutonic	Permian-Triassic
PPR12-04 ^b	3987	-14.00762	-70.07671	plutonic	Permian-Triassic
PPR12-05 ^b				•	Permian-Triassic
	4576	-14.02176	-70.10729	plutonic	
PPR12-06 ^b	4764	-14.04273	-70.15513	plutonic	Permian-Triassic
PR11b	4641	-13.95748	-70.31457	plutonic	Permian-Triassic
IPR12 ^b	4507	-13.91993	-70.30699	plutonic	Permian-Triassic
IPR14 ^b	4084	-13.89674	-70.23135	plutonic	Permian-Triassic
PPR12-13 ^b	414	-13.18958	-70.38836	quartzite	Lower Cretaceous
				-	
IPR29 ^b	530	-13.21110	-70.36470	quartzite	Lower Cretaceous
IPR30 ^b	430	-13.22480	-70.35720	quartzite	Lower Cretaceous
PR04 ^c	4657	-13,49533	-71.14618	granite	Permian-Triassic
AR-13 ^d	4600	-13.96583	-70.33333	monzogranite	Permian-Triassic
	3850	-14.00556	-70.03667	monzogranite	Permian-Triassic
OCA-268 ^d					

Note: Formation ages are based on 1:100,000 map quadrangles (INGEMMET, 2022) and field observations in case the geologic contacts differed from those published.

^a Samples from Lease and Ehlers (2013).

^b Samples from Perez et al. (2016a).

^c Sample from Perez and Levine (2020).

d Samples from Kontak et al. (1990). Sample elevations were estimated based on the samples' coordinates and a 90-m digital elevation model.

Table 2Summary of new and previous bedrock thermochronometric ages.

Sample	Eleva- tion (m)	AHe age (Ma)	AHe 1s err. (Ma)	n	AFT central age	AFT 1s err. (Ma)	N	ZHe age (Ma)	ZHe 1s err. (Ma)	n	ZFT central age	ZFT 1s err. (Ma)	N
	(/		()		(Ma)	()			()		(Ma)	(/	
San Gabán (a	long transect	from SW to N	E)										
18PE71	3939	11.1	3.4	4/4	-	-		_	-		_	_	
18PE70	4017	19.1	4.5	3/3	*				-		-	_	
18PE68	3954	2.7	0.7	1/1	_	-		\sim 25-84		4	-	-	
18PE66	4285	22.1	1.6	3/3	_	_		\sim 87–248		4	_	_	
18PE65	4222	\sim 24-41		5	-	-		-	-		-	-	
18PE64	4185	~17-31		5	-	-		-	-		-	-	
11PR25	4161	$\sim 3-46^{a}$		3	-	-		\sim 73–109 ^a		3	-	-	
18PE06	3791	6.2	1.5	1/1	21.9	4.6	8	31.2	2.5	3/3	_	_	
11PR16	3240	4.0 ^a	0.2	3/3	50.3	14.2	13	_	-		-	-	
18PE62	4373	15.6	1.5	4/4	16.5	1.6	19	-	-	1/1	_	_	
11PR09	2775	4.1 ^a	0.8	3/4	8.3	1.1	23	75.5ª	17.4	1/1	-	_	
11PR11	2974	3.9 ^a	2.3	7/7	-	-		-	-		-	_	
18PE07 11PR05	2775 2056	1.9 2.8 ^a	1.3 0.8	4/4	- 8.2	0.8	22	- 15.6 ^a	- 1.3	3/3	- 28.8	2.6	9
18PE08	2030	4.3	0.8	5/5 4/4	o.2 _	U.0 -	22	15.6"	1.5 -	3/3	20.0 -	2.0 -	9
11PR04	1759	3.7ª	0.3	4/4	8.0	0.6	22	- 15.6 ^a	0.6	3/3	_	_	
11PK04 18PE09	1759	4.2	1.0	4/4 4/4	8.U -	0.6 -	22	15.6"	0.0 -	درد	_	_	
11PR01	1562	4.2 4.3 ^a	0.6	4/4	9.7	- 1.1	25	_ 15.0 ^a	2.6	3/3	- 36.5	2.3	20
18PE10	1134	5.7	2.2	4/4	9.7 7.3	0.6	23	13.5	1.4	3/3 4/4	34.2	2.5	2:
18PE10	858	3.9	0.9	4/0 1/1	7.5 8.0	0.0	20	15.5	1. 4 -	-1/-1	54.Z -	- -	2.
18PE13	484	3.5	0.9	4/5	-	-	20	39.1	3.8	3/4	_	_	
18PE17	407	47.1	11.3	1/1	_	_		-	-	3/4	_	_	
11PR30	430	~3-38ª	11.5	4	_	_		_	_		_	_	
11PR29	530	$\sim 2-9^{\rm b}$		5	_	_		_	_		_	_	
NPPR12-13	414	$\sim 0.3 - 9^{b}$		5	_	_		_	_		_	_	
18PE18	359	~12-31		4	_	_		~26-284		4	_	_	
				•				20 20 1		•			
Marcapata (al	ong transect	from SW to NI	Ε)										
18PE53	4138	9.6	1.6	4/4	_	-		-	-		-	-	
18PE52	3605	3.3	0.5	3/3	25.7	3.7	21	\sim 42–89		4	_	-	
18PE55	3963	13.3	3.2	1/1	-	-		-	-		-	-	
18PE57	4251	\sim 9–29		3	-	-		-	-		-	-	
18PE61	5042	17.2	3.0	3/4	-	-		19.0	3.2	1/1	-	-	
18PE05	4524	10.8	2.6	1/2	_	_		36.9	3.7	2/2	_	_	
18PE04	4731	15.5	2.2	3/4	16.6	2.9	20	\sim 28–48		3	_	_	
06JBPR19	4269	5.8	2.3	2/2	_	-		-	-		-	-	
18PE33	3988	~2;		2		-		-	-		-	-	
OCIDDD17	2071	~18	0.4	2/2									
06JBPR17	3971	4.8	0.4	2/2	- 7.4	-	10	-	-	4/4	-	-	
18PE32	3367	3.5	1.4	4/4	7.4	1.1	19	7.3	0.8	4/4	27.3	2.6	14
18PE29	2603	1.6	1.0	4/4	-	-		4.1	0.3	4/4 6	14.3 -	1.7	9
17PR04	4657	12.2°	0.9 0.4	6/6	- 3.3	- 0.3	22	~39-69°	0.5	3/3		1.4	13
18PE28	2416	1.3 2.2		4/4			23	5.5		3/3	16.7	1.4	1.
18PE27	2289		1.0	4/4	- 101	10	21	-	12	414	_	-	
18PE03 18PE02	4337 4537	10.1 15.4	2.9 2.2	4/5 5/5	10.1 -	1.9 -	21	33.8 ~20-104	1.3	4/4 4	_	_	
18PE26	1935	3.0	0.3	5/5	_ _	_			1.4	4/4	_	_	
06 BPR10	1933	1.4	0.3	2/2	8.6	- 1.5	14	6.8	1. 4 -	-1/-1	32.5	7.7	3
оојъркто 18PE23	959	2.6	0.6	2/2 4/4	9.3	1.6	24	7.8	1.9	3/3	28.9	2.6	1
18PE22	851	-	-	-1/-1	13.8	2.1	27	15.8	1.7	1/1	-	2.0	1
18PE21	754	_	-		-	Z.1 -	21	16.9	0.5	3/3	36.6	2.0	2
18PE20	709	7.6	2.7	6/6	*			-	-	3/3	-	-	2
				5,0									
Tres Cruces (a	along transect	from SW to N	NE)										
18PE73	4096	14.1	4.2	4/4	37.2	2.9	22	-	-		-	-	
18PE35	3772	4.8	1.5	5/5	26.6	7.7	7	~81-611		4	_	=	
18PE51	2993	8.7	2.1	1/1	-	-		_	_		-	_	
18PE36	2920	4.9	0.8	2/2	-	-		-	-		-	-	
18PE37	3490	4.2	0.2	2/3	-	-		_	_		-	_	
	2176	17.2	4.1	1/1	-	-		-			-	-	
18PE39	1924	2.5	0.6	1/1	-	-		_	-		-	-	
	1324		4.4	4/4 ,	*			7.9	1.0	3/4	20.7	2.0	2
18PE47	1828	3.6	1.1	-1/- /									
18PE47 18PE40		2.1	0.1	3/3/	*			_	_	,	-	-	
18PE47 18PE40 P04x-31	1828				* 9.9	2.5	12	8.5	- 0.9	4/4			1
18PE39 18PE47 18PE40 PO4x-31 18PE41 18PE43	1828 1750 1420 655	2.1 2.2 9.2	0.1 0.1 1.8	3/3/ 5/5 3/4		2.5 2.7	12 21			•	_	-	1
18PE47 18PE40 P04x-31 18PE41	1828 1750 1420	2.1 2.2	0.1 0.1	3/3/ 5/5	9.9			8.5		4/4	- 16.0	- 1.5	1

(continued on next page)

Table 2 (continued)

•	Eleva-	AHe age	AHe	n	AFT	AFT 1s	N	ZHe age	ZHe 1s	n	ZFT	ZFT 1s	N
	tion	(Ma)	1s err. (Ma)		central age (Ma)	err. (Ma)		(Ma)	err. (Ma)		central age (Ma)	err. (Ma)	
	(m)												
Eastern Coasa	Pluton area	(with decreasing	ng elevation)	ı									
NPPR12-06	4764	26.5 ^b	9.3	4/5	-	=.		34.3 ^b	4.4	3/3	-	=	
NPPR12-05	4576	16.4 ^b	0.4	4/4	-	-		26.9 ^b	1.4	3/3	-	_	
NPPR12-04	3987	17.1 ^b	5.2	4/5	-	-		23.1 ^b	1.0	3/3	-	_	
COCA-270	3970	_	-		28.8 ^d	4.9		_	_		_	_	
NPPR12-01	3950	11.1 ^b	3.4	3/4	16.3	1.9	14	18.6 ^b	1.1	3/3	_	_	
COCA-268	3850	_	-		18.4 ^d	3.1		_	_		_	_	
NPPR12-03	3802	11.3 ^b	1.6	4/4	9.2	2.0	7	21.6 ^b	1.4	3/3	_	_	
NPPR12-02	3710	10.5 ^b	0.5	2/4	13.4	1.2	22	21.2 ^b	1.6	3/3	-	-	
Western Coas	a Pluton area	a (with decreasi	ng elevation	1)									
14PR11	4641	30.5 ^b	5.1	3/3	_	_		_	_		_	_	
BAR-13	4600	_	-		19.9 ^d	3.4		_	_		_	_	
14PR12	4507	11.6 ^b	1.4	3/3	_	_		30.5 ^b	3.0	3/3	_	_	
14PR14	4084	_	-		_	_		32.8 ^b	2.8	3/3	_	_	

Note: Apatite and zircon (U-Th)/He (AHe and ZHe, respectively) ages and errors are weighted mean ages and 1 weighted standard deviation unless otherwise noted. For partially reset and unreset samples, the range of single-grain ages is given. If only one single-grain age is available, the single-grain age is presented with an average analytical uncertainty (see also Tables S1 and S2).

For consistency of data presentation and in light of new data from some of the previous samples, we re-evaluated and recalculated previous (U-Th)/He ages when possible. Previous data:

- ^a Lease and Ehlers (2013), single-grain and weighted mean ages were recalculated.
- b Perez et al. (2016a), mean ages were re-evaluated based on new AFT data and recalculated.
- ^c Perez and Levine (2020), weighted mean ages were calculated.

models (to reach an equilibrium state) followed by 200,000 postburn-in models, or more if model convergence was not achieved.

4. Results

4.1. Observed timing of exhumation

In the following, thermochronometric results are presented by transect and tectonomorphic region (plateau, plateau edge/interfluves, canyon bottoms, and Subandes). A summary of new and previous ages is given in Table 2, and single-grain data are reported in the associated data publication (Tables S1–S5, Falkowski and Ehlers, 2023). Note that only one AHe or ZHe single-grain analysis is available for some samples due to low apatite/zircon yields (Table 2). Supplementary Text S1 and Tables S1 and S2 report our interpretation of those and other samples' state of resetting, as well as data evaluation criteria. Furthermore, some fission-track samples yielded only a few datable grains; hence, some ages have relatively large uncertainties (e.g., 06]BPR10 ZFT; Table 2).

4.1.1. San Gabán transect

Fig. 2 shows sample locations along a topographic swath profile through the San Gabán transect (Fig. 1 for location), thermochronometric ages along the profile, and the balanced cross-section of Perez et al. (2016a). In the backthrust belt, reset AHe ages increase from \sim 11 Ma to \sim 22 Ma from the southwest to the northeast (cf., Figs. 2b, 2c). The \sim 3 Ma AHe single-grain age of 18PE68 in between this trend might be an outlier based on its deviation from the regional trend. Farther to the northeast, in the Macusani Structural Zone, three AHe ages are partially reset, with a northeastward trend of increasingly younger single-grain age ranges (\sim 24–41 Ma to \sim 3–46 Ma; Figs. 2b, 2c, Table 2). The three ZHe samples from the plateau area are unreset or partially reset and reflect the same trend as the AHe ages.

To avoid adding elevation-dependence (i.e., interfluve vs. canyon bottom samples) to Fig. 2b, we show from the canyon's upper

reaches and the northeastern part of the Macusani Structural Zone only samples from minimum elevations. The excluded sample (hollow circle, Fig. 2a) and those marked by the orange rectangle in Fig. 2b are shown in Fig. 3. From the plateau edge and down the canyon, AHe ages are young and relatively consistent (\sim 3–6 Ma, one \sim 2 Ma age). In contrast, AFT and ZHe ages are older at the plateau edge (partially reset ZHe single-grain ages \geq 73 Ma and one reset ZHe age of \sim 31 Ma, and AFT ages of \sim 22 and \sim 50 Ma) and become younger farther down in the canyon (Fig. 2b). In the canyon, the ages are consistent (ZHe \sim 15 Ma, and AFT \sim 8 Ma), particularly for samples at elevations below \sim 2500 m (Fig. 3). ZFT ages from the canyon bottom are \sim 29–37 Ma (Figs. 2b, 3a).

Toward the lower-relief (<1 km compared to ≥ 2.5 km; Fig. 2a) foreland, one AHe age is ~ 4 Ma, while the same sample's ZHe age is ~ 40 Ma (18PE13; Fig. 2b, Table 2). In the Subandes, AHe ages are partially reset, ranging from ~ 0.3 Ma to ~ 47 Ma, and one ZHe sample from Oligocene–Miocene strata is unreset ($\sim 26-284$ Ma single-grain ages; Fig. 2b, Table 2).

Overall, AHe, AFT, and ZHe ages from the plateau edge to the Subandes show a "U-shape" where the youngest ages are in the middle and become older and partially reset or unreset toward the sides (dashed line at \sim 110–170 km, Fig. 2b). The middle part is relatively flat and wide (at least 50 km for AHe). There are too few ZFT ages to see whether this thermochronometer system also reflects this trend. Finally, it is noticeable that samples from the plateau edge have variable ZHe age resetting (\sim 31 Ma reset ZHe age of 18PE06 compared to partially reset samples 11PR25 and 11PR16; Figs. 2a, 2b, 3a). This variability indicates that at around 30 Ma samples resided close to ZHe closure temperatures.

The Coasa Pluton area is located at the plateau edge where the San Gabán transect has a lateral offset (Fig. 1). These samples constitute a \sim 1000-m quasi-vertical profile. Nine samples from 3710–4764 m elevation have AHe and ZHe ages ranging from 10.5 \pm 0.5 Ma to 26.5 \pm 9.3 Ma and 18.6 \pm 1.1 Ma to 34.3 \pm 4.4 Ma, respectively (Table 2, Fig. 4; Perez et al., 2016a). New AFT ages from three of those samples from 3802–3950 m range from 9.2 \pm 2.0 Ma

n: Number of single-grain ages used to calculate the weighted mean/total number of single-grain ages available (see Tables S1 and S2 for details).

N: Number of grains dated (see Tables S3-S5 for details).

^{*}Uranium concentration is too low for AFT dating.

^d Kontak et al. (1990), acquired AFT data with the population method; biotite 40 Ar/ 39 Ar ages from the same samples range from 179±1.8 to 207±2.2 Ma.

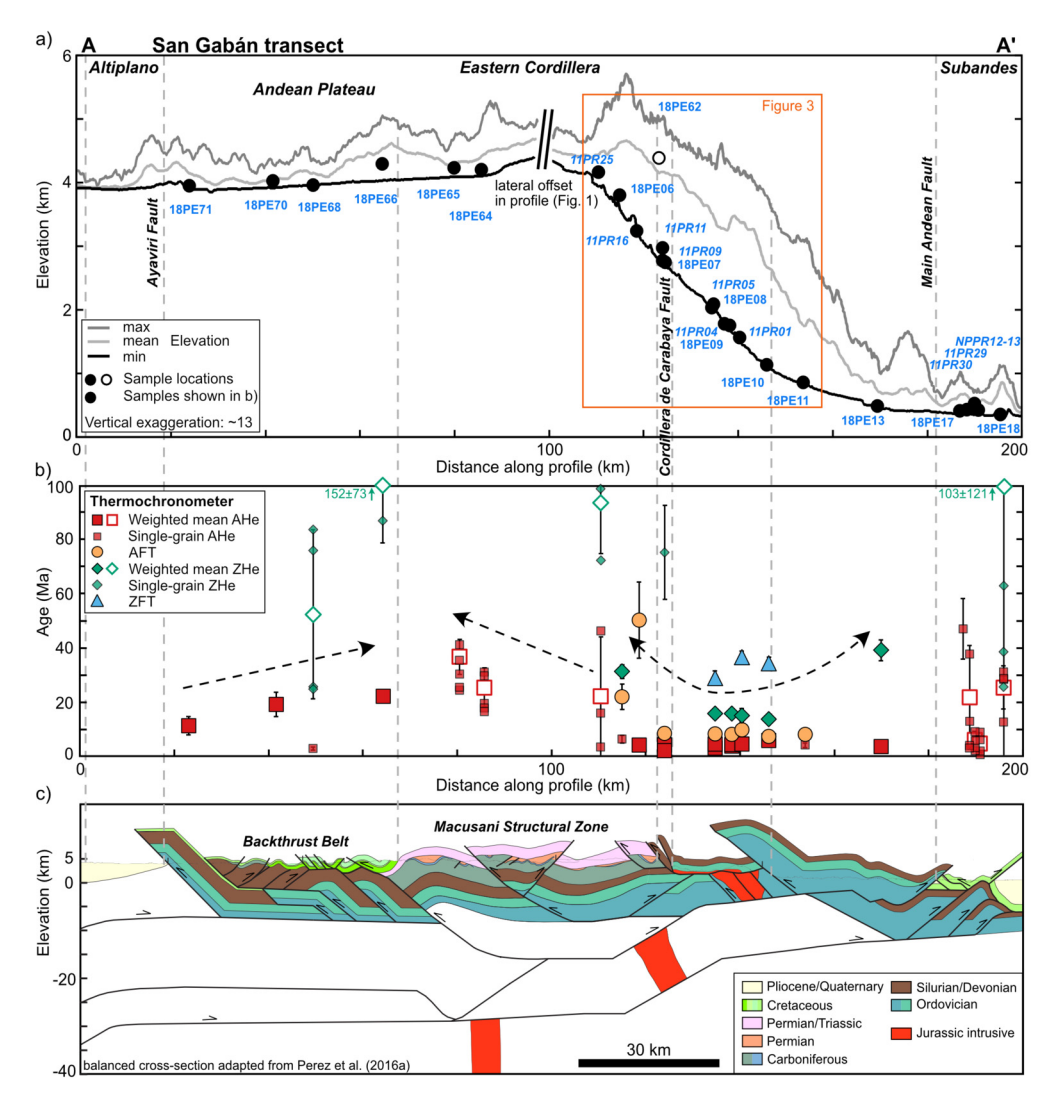


Fig. 2. Topographic swath profile A-A' (a), thermochronometric ages along the profile (b), and balanced cross-section (simplified from Perez et al., 2016a) of the San Gabán transect (see Fig. 1 for location). (a) also shows sample locations and names (previous samples are in italics, see Table 1 for references). For comparison between panels, the gray dashed lines connect the projected sites where main faults break the surface. Reset AHe and ZHe weighted mean ages and AFT and ZFT central ages (1σ -errors) are plotted with filled symbols, while partially reset or unreset AHe and ZHe ages are plotted with unfilled symbols and additional single-grain ages with smaller and transparent symbols (b).

to 16.3 ± 1.9 Ma (Table 2, Fig. 4). Three previous AFT samples from 3850-4600 m elevation range from 18.4 ± 3.1 Ma to 28.8 ± 4.9 Ma (Table 2, Fig. 4; Kontak et al., 1990). Biotite 40 Ar/ 39 Ar ages from those three samples range from $\sim180-208$ Ma (Kontak et al., 1990) and are not shown for clarity. Overall, thermochronometer ages increase with increasing elevation. Between ca. 3700 and 3950 m elevation, AHe and ZHe ages show a steep age increase at ~11 Ma and ~22 Ma, respectively. However, we cannot determine a statistically significant break-in-slope in these ages (following the approach of Glotzbach et al., 2011). This is due to the range in ages, considerable uncertainty in some ages, and a sample gap at $\sim4100-4500$ m elevation. Section 4.2.2 discusses thermal history models for multi-thermochronometer samples from the eastern part of the profile, where more samples are available.

4.1.2. Marcapata transect

Fig. 5 shows results from the Marcapata transect. The location of samples in relation to structures and tectonomorphic regions is similar to the San Gabán transect. However, here, one sample is also located in the Altiplano Basin, one at the Ayaviri Fault, and no samples in the Subandes.

Thermochronometer age trends are the same as on the San Gabán transect. In the backthrust belt, AHe ages increase northeastward from \sim 3 Ma to partially reset single-grains of \sim 9-29 Ma (Fig. 5b, Table 2). From the plateau edge to the foreland (\sim 100–180 km in Fig. 5b), we observe a "U-shape" pattern (dashed line in Fig. 5b) that is also suggested by the ZFT ages. Thermochronometer ages that form the "U-shape" are generally younger, and the age difference between thermochronometers is smaller than on the San Gabán transect (Figs. 5b-d, Table 2). The youngest AHe ages in the canyon are \sim 1–3 Ma and increase to 11 Ma and 17 Ma in the upper reaches of the canyon and ~ 8 Ma toward the Subandes (Fig. 5b). Youngest canyon ZHe ages increase from \sim 4-8 Ma to \sim 19 Ma and \sim 37 Ma to the southwest, and \sim 16–17 Ma to the northeast (Fig. 5b). The youngest ZFT ages are \sim 14 Ma and \sim 17 Ma and increase to \sim 27 Ma to the southwest and \sim 37 Ma to the northeast (Figs. 5b, 5c, Table 2).

Marcapata interfluve samples (18PE02 to -05, \sim 4300–4700 m) are from similar elevations to samples from the Coasa Pluton, located about 100 km to the southeast (Fig. 1). Marcapata interfluve and Coasa Pluton samples have similar AHe ages (\sim 10–15 Ma) and in both regions, same-sample AHe and AFT ages are identical within error (Table 2, Figs. 4 and 5c, 5d).

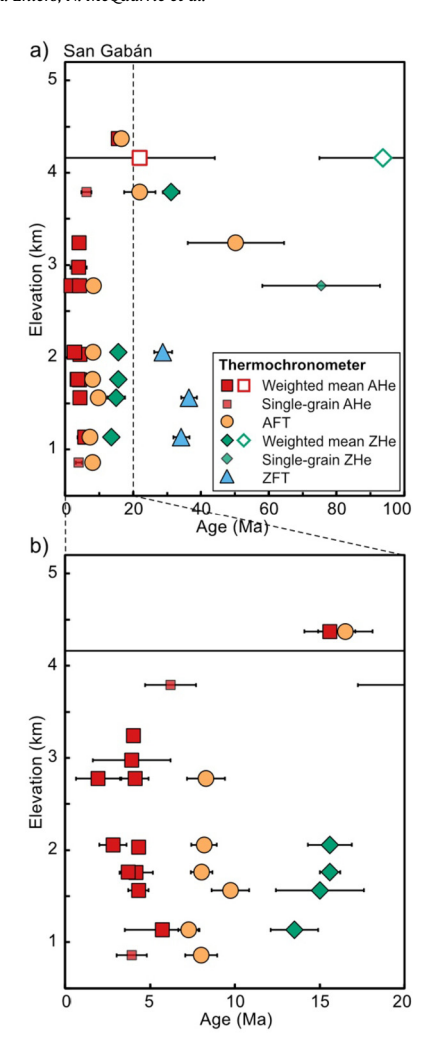


Fig. 3. Thermochronometric age-elevation plot of San Gabán canyon bottom and plateau edge/interfluve samples (samples marked with an orange box in Fig. 2a) with all ages (a) and <20 Ma ages (1σ -errors) for detail (b). The symbols for ages are the same as in Fig. 2b, but partially reset AHe and ZHe ages are not shown with single-grain ages. If only one single-grain age is shown, it is the only one available for that sample (cf., Table 2).

4.1.3. Tres Cruces transect

As seen in the topographic swath (Fig. 6a) and the topographic map (Fig. 1), the Tres Cruces profile differs from the previous two in that the sampled canyon has a lower relief (<2 km) and the plateau edge is less well-defined by interfluves. This difference is due to the transects' proximity to the Abancay Deflection and the large-magnitude river incision that trends northwest-southeast. Due to overall poorer apatite and zircon yield from the Tres Cruces samples compared to the other transects, fewer thermochronometric ages are available. Still, similar general trends and ages as in the Marcapata transect are suggested. From the Ayaviri Fault, AHe ages increase from \sim 5 Ma to \sim 14 Ma and \sim 9 Ma (one single-grain age) to the southwest and northeast, respectively. The ZHe sample from close to the fault is partially reset, the AFT age is \sim 27 Ma (\sim 26 Ma in the Marcapata transect; Table 2, Fig. 5b). Toward the southwest, the AFT ages increase to \sim 37 Ma (Fig. 6b). The youngest AHe, AFT, and ZHe ages in the canyon are \sim 2-4 Ma, \sim 10 Ma, and \sim 8-9 Ma, respectively, and increase to \sim 9-15 Ma, \sim 21 Ma, and 34-55 Ma, respectively, toward the Subandes (Table 2, Fig. 6b). The \sim 17 Ma AHe single-grain age might be an outlier based on its deviation from the regional trend (18PE39, Figs. 6b, 6c). The upper canyon area, where thermochronometric ages would be expected to increase like on the other transects, is either not sampled (sample

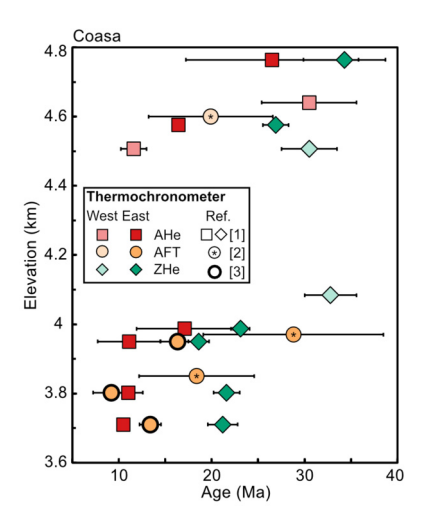


Fig. 4. Thermochronometric age-elevation plot of western and eastern Coasa Pluton samples (see Fig. 1 for location). References are [1] Perez et al. (2016a), [2] Kontak et al. (1990), and [3] this study. Errors are 1σ , except for AFT ages (2σ) from Kontak et al. (1990) since those ages were acquired with the population method. For consistency with interpreting other ages, we consider the lower 2σ -age range of COCA-270 (3970 m) closer to the true age. Note that one new AFT age (NPPR12-03, 9.2±2.0 Ma, Table 2) is, within 1σ -error, identical to the sample's AHe age (11.3±1.6 Ma, Table 2). The AFT age has a relatively high uncertainty, given that only seven grains could be dated. We consider the upper 1σ -age range to be closer to the true age.

gap between ~ 90 and 110 km, Figs. 6a, 6b), not present in this transect, or not captured by the AHe ages around 120 km on the profile ($\sim 4-5$ Ma, Fig. 6b). The plateau incision from the northwest (at ~ 4 Ma; Gérard et al., 2021a) might have influenced those AHe ages. Finally, two ZFT ages from the canyon bottom are ~ 21 Ma and ~ 16 Ma, similar to Marcapata Canyon ZFT ages (Figs. 5b, 6b).

4.2. Inverse thermal history modeling

For brevity, we present in Fig. 7 a synthesis of the inverse thermal history modeling results by their tectonomorphic region. Only selected thermal histories from representative samples with multiple thermochronometers are shown for clarity. All thermal history models conducted are shown in Figs. S2 (with axes clipped as in Fig. 7) and S3 (unclipped models, with relative probability) that include inset plots of observed vs. predicted ages. Model input, settings, and ages are provided in Table S6. Only a few thermal histories are available for the Tres Cruces transect, which means the entire range in thermal histories is not recovered. The following summarizes the main observations of the thermal histories from 50–0 Ma.

4.2.1. Thermal histories of plateau samples

The coolest maximum temperatures were generally experienced by the sedimentary rock samples from the plateau portion of the Eastern Cordillera. ZHe ages are not reset here, and time-temperature paths are typically below $180\,^{\circ}\text{C}$ (Fig. 7a). Moreover, some AHe ages are not fully reset. This indicates maximum temperatures were mostly below $\sim\!68\,^{\circ}\text{C}$ in the Macusani Structural Zone (at least of the San Gabán transect) and the northeastern end of the backthrust belt (at least of the Marcapata transect) where samples are available (18PE64 and 18PE57; Fig. 7a). Initial, slow cooling of some samples to $\sim\!50\,^{\circ}\text{C}$ possibly occurred at $\sim\!40\,^{\circ}\text{Ma}$ (18PE64, 18PE57; Fig. 7a) and before $\sim\!20\,^{\circ}\text{Ma}$ (18PE70; Fig. 7a), while other samples at the southwestern margin of the backthrust belt remained at temperatures around $100\,^{\circ}\text{C}$ (18PE35; cf., Figs. 6a, 7a) or cooled very slowly (18PE52; cf., Figs. 5a, 7a) until they cooled more rapidly to surface temperatures after $\sim\!5\,^{\circ}\text{Ma}$.

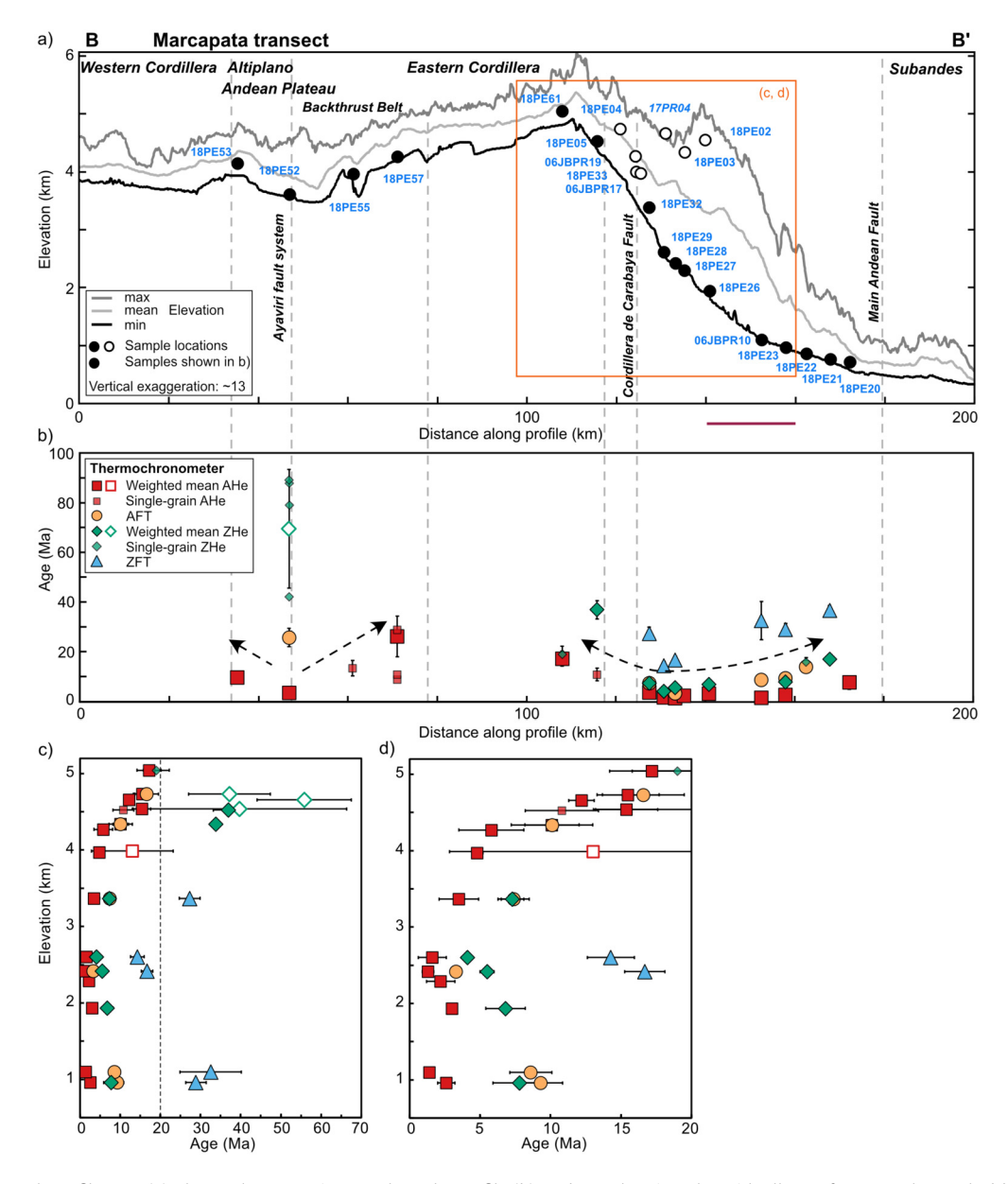


Fig. 5. Topographic swath profile B-B' (a), thermochronometric ages along the profile (b), and age-elevation plot with all ages from samples marked by the orange box in panel a (c), and <20 Ma ages (1σ -errors) for detail (d) of the Marcapata transect (see Fig. 1 for location). (a) also shows sample locations and names (previous sample in italics from Perez and Levine, 2020). For comparison between panels a and b, vertical gray dashed lines connect the projected sites where main faults break the surface. Data symbols of (b) and (c, d) as in Fig. 2b and 3, respectively.

4.2.2. Thermal histories of plateau edge/interfluve samples

Maximum paleo-temperatures of samples from the plateau edge were higher than those of plateau samples (Figs. 7a, 7b). Depending on location and elevation, some samples experienced temperatures below ZHe closure over the past 50 Myrs (e.g., 17PR04 and 18PE62, both are high-elevation interfluve samples; Figs. 2a, 5a, 7b), while others cooled below ZHe closure temperatures at $\sim\!35$ Ma or $\sim\!25$ –20 Ma. Most samples then cooled rapidly to below AHe closure temperatures at $\sim\!15$ Ma or $\sim\!12$ –8 Ma (Fig. 7b). Note that the $\sim\!50$ –15 Ma part of the 17PR04 thermal history and all samples' thermal histories above ZHe closure temperatures are not (well) constrained because of lacking AFT and ZFT data, respectively (Table 2, Fig. 7b).

The Coasa Pluton models fit the San Gabán and Marcapata interfluve models well (Fig. 7b), indicating that an elevation-dependence of cooling ages can explain the other models' variability, i.e., samples resided at different depths but experienced the same cooling history. Without ZFT data, the onset of cooling

is not well constrained (possibly ${\sim}40{\text -}35$ Ma), but rapid cooling was underway by ${\sim}22$ Ma. It is unclear whether cooling was continuous until ${\sim}8$ Ma or episodic with a ${\sim}22{\text -}15$ Ma and a ${\sim}12{\text -}8$ Ma phase.

4.2.3. Thermal histories of canyon bottom samples

The earlier thermal history of samples from the upper reaches of the canyons appears similar to the plateau edge thermal history (e.g., 11PR16 and 18PE06, Fig. 7c). The later (<10 Ma) thermal history of all canyon bottom samples is distinctly different from the plateau (edge) samples. The plateau (edge) samples were below AHe closure temperatures, while the canyon bottom samples were hotter than ZHe or ZFT closure temperatures after 20 Ma or even after 10 Ma. Generally, cooling occurred since at least \sim 35 Ma, and phases of accelerated cooling occurred between ca. 25 and 15 Ma, around 10 Ma, and after \sim 5 Ma (Figs. 7c, S3). Compared to the plateau (edge) samples, thermal histories of canyon samples suggest some along-strike variability, reflecting the thermochronome-

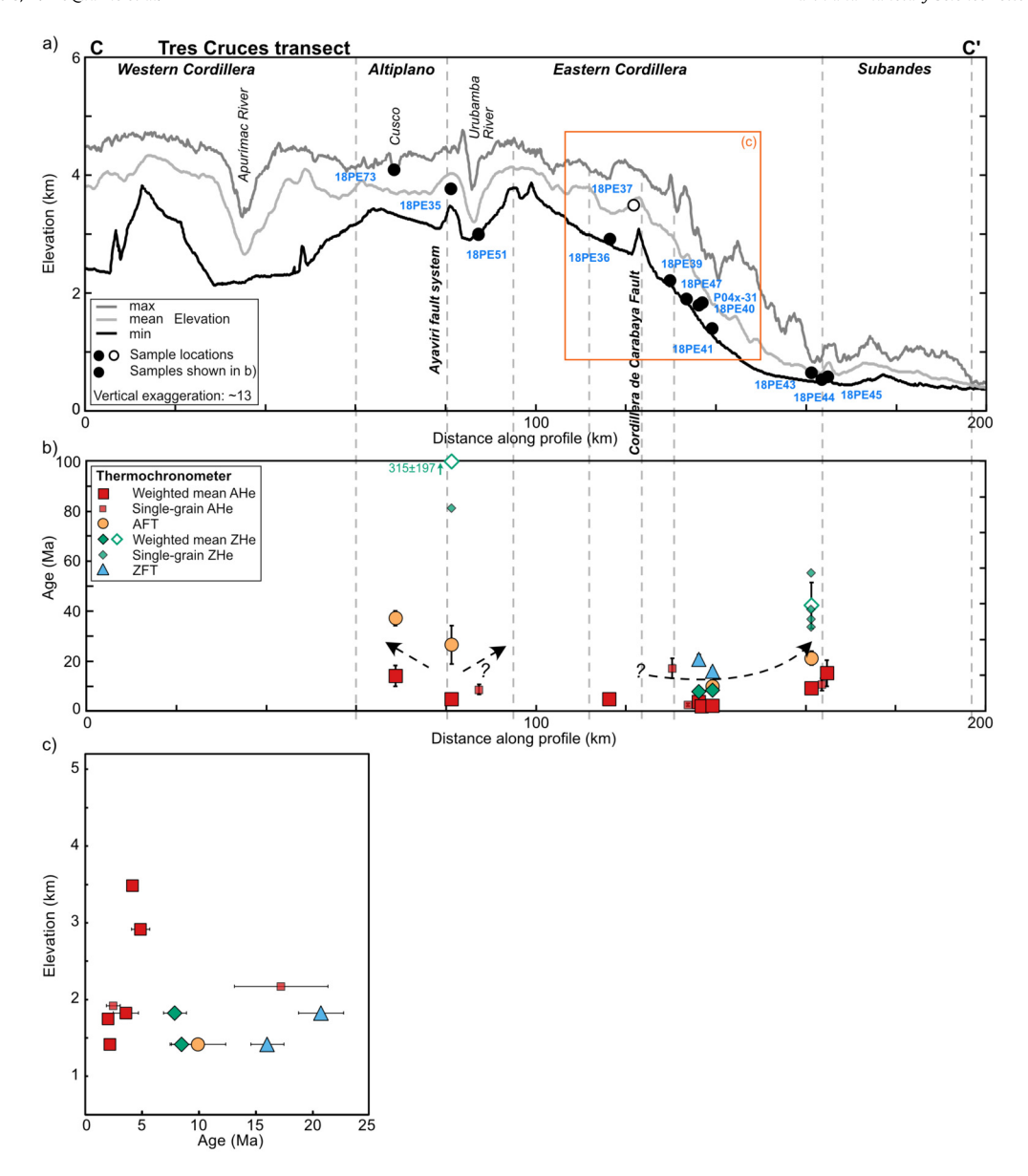


Fig. 6. Topographic swath profile C–C' (a), thermochronometric ages along the profile (b), and age-elevation plot with all ages $(1\sigma$ -errors) from samples marked by the orange box in panel a (c) of the Tres Cruces transect (see Fig. 1 for location). (a) also shows sample locations and names. For comparison between panels a and b, vertical gray dashed lines connect the projected sites where main faults break the surface. Data symbols of (b) and (c) as in Fig. 2b and 3, respectively.

ter observations (Section 4.1). Fig. 8 shows this variability in more detail for representative thermal histories. More thermal histories are shown in Fig. 8 compared to Fig. 7c because details can be seen better here.

Within the temporal resolution of the data, the San Gabán thermal histories show minimal downstream variability (Figs. 8a, S2, S3). Samples cooled from increasingly higher temperatures from the upstream-most ($\sim\!70\,^{\circ}\text{C}$) to downstream-most ($\sim\!140\,^{\circ}\text{C}$) sample. Except for the upstream-most samples shown (18PE06, 11PR09), the results show a rapid cooling phase at $\sim\!4$ Ma, which corroborates the findings of Lease and Ehlers (2013). At that time, samples cooled from $\sim\!100\,^{\circ}\text{C}$ to below AHe closure temperatures and, consequently, cooling between then and present-day is not resolvable. Similarly, whether the upstream-most samples also experienced cooling (of relatively small magnitude) at $\sim\!\!4$ Ma (and potentially later) is not resolvable.

Cooling of the Marcapata Canyon samples appears less consistent since 10 Ma (Figs. 8b, S3). The upstream-most sample shown in Fig. 8b experienced rapid cooling at \sim 8 Ma to <100 °C be-

fore cooling to surface temperatures started between \sim 2.5 and 2 Ma. Most samples indicate an accelerated cooling phase sometime between \sim 6 and \sim 3 Ma. This timing of cooling is similar to the San Gabán Canyon cooling but is from higher temperatures $(\sim190-130\,^{\circ}\text{C})$ to $\sim100-60\,^{\circ}\text{C}$. Furthermore, another (younger) cooling phase is resolved from the AHe data starting at \sim 2-1 Ma (Fig. 8b, Table 2). In contrast to the San Gabán samples, there seems to be no consistency in that higher-elevation samples would be cooled from lower temperatures and lower-elevation samples from higher temperatures (Fig. 8b). For example, samples 18PE29 and 18PE28 differ only by 200 m in elevation (Table 2) and <4 km in lateral distance, but their thermal histories suggest a temperature difference of ${\sim}80\,^{\circ}\text{C}$ at 5 Ma (Fig. S3). In the absence of a local heat source, this is unrealistic and illustrates the limit of data resolution and model fits. We focus on general trends to avoid overinterpreting the model results.

The two modeled thermal histories of the Tres Cruces Canyon are consistent in showing a rapid cooling phase to temperatures just below 100 °C at 10–8 Ma, followed by slow cooling before

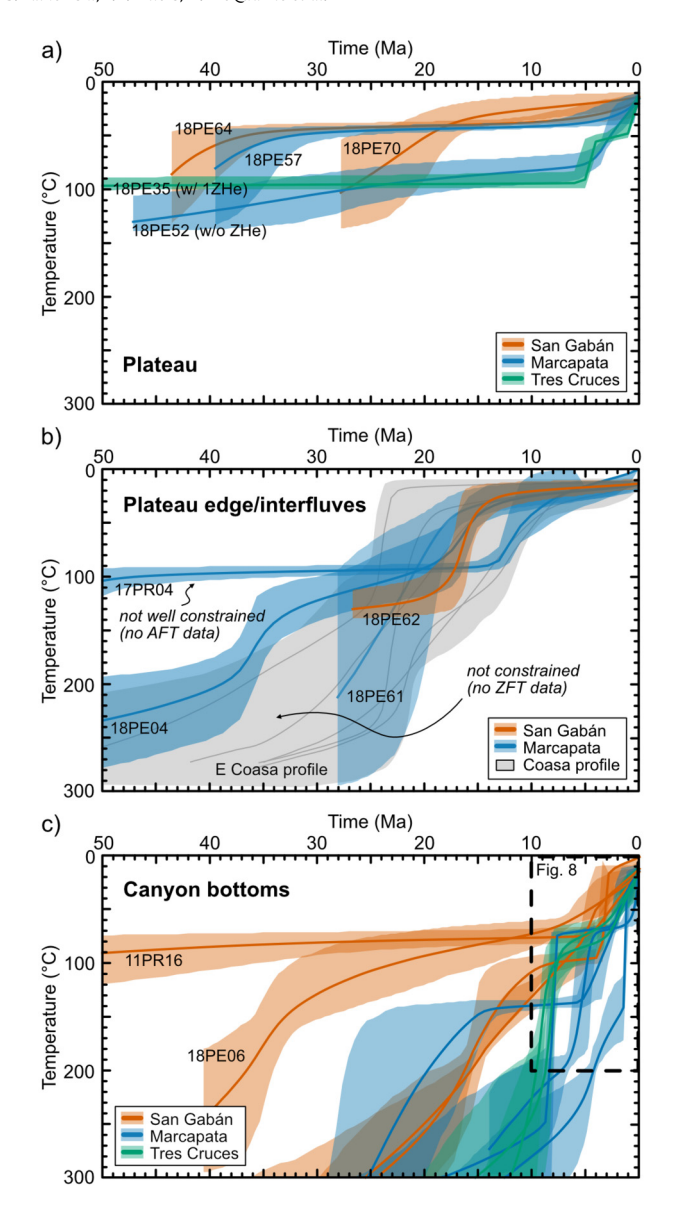


Fig. 7. Representative inverse thermal models of samples from the plateau (a), the plateau edge/interfluves (b), and the canyon bottoms (c). In c, only sample names mentioned in the text are shown for readability. The solid lines with transparent bands represent the *expected models* from *QTQt* thermal histories, whereby the solid lines represent the weighted average of all accepted models (weighted by the posterior probability of each model) with 95% credible intervals (transparent band). For the eastern Coasa Pluton elevation profile (cf., Fig. 4), the envelope of all samples' thermal models (gray band) and individual weighted average models (thin gray lines) are shown (b). Sample NPPR12-01 from the Coasa profile is excluded from the thermal histories envelope as it seems to represent an outlier (Table 2). For all thermal history models conducted, see Figs. S2 and S3, and Table S6.

final cooling from ${\sim}80\text{--}70\,^{\circ}\text{C}$ to surface temperatures since ${\sim}4\text{--}3$ Ma (Fig. 8c).

5. Discussion

5.1. Synthesis of exhumation timing and along-strike variations

Rocks now exposed on the plateau experienced limited Cenozoic exhumation since $\sim\!40$ Ma (or possibly earlier). In the backthrust belt, a phase of exhumation began between 30 and 20 Ma and continued slowly, or possibly episodically, with increasingly younger exhumation toward the southwest, where the youngest episode of exhumation from depths with temperatures $<\!100\,^{\circ}\text{C}$ began $\sim\!5\text{-4}$ Ma (Figs. 2, 5, 6, 7a).

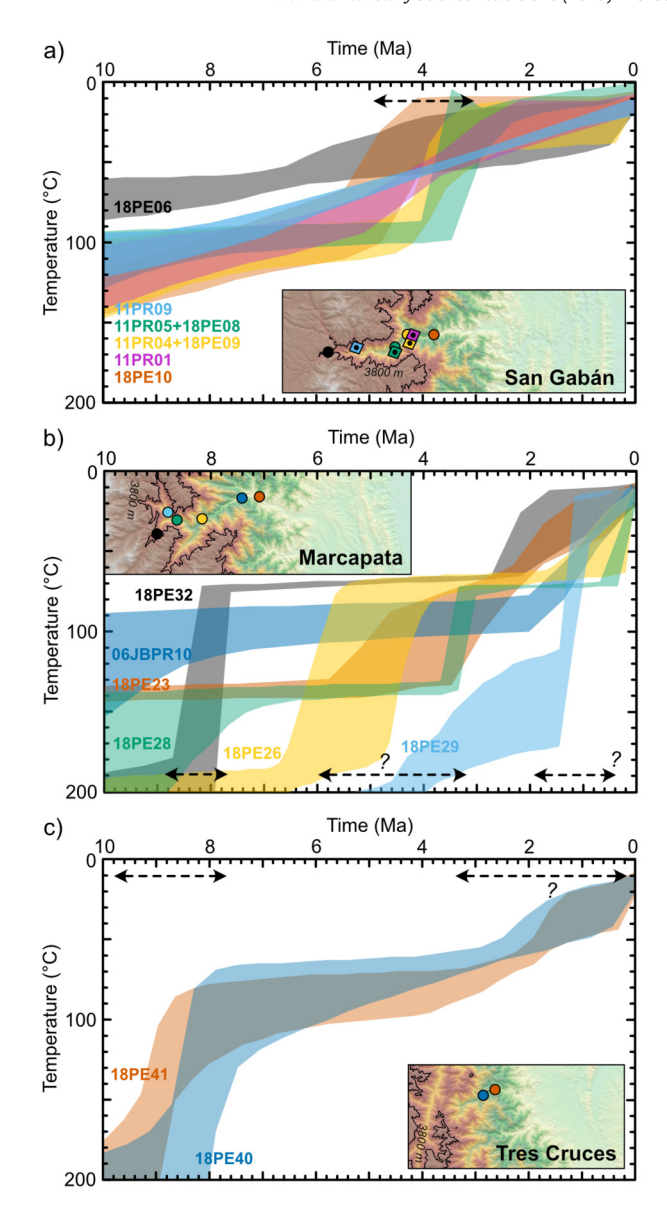


Fig. 8. Most recent cooling (exhumation) phases of canyon bottom samples. The panels show details of representative *QTQt* inverse thermal models of canyon bottom samples from the San Gabán (a) and Marcapata (b) transects, and the two available thermal models of canyon bottom samples from the Tres Cruces transect (c). Note that more samples' thermal histories are shown than in Fig. 7c due to the better readability of details here. Inset maps show color-coded locations of samples shown in the time-temperature plots; sample symbols (circles, diamonds) as in Fig. 1. The dashed lines with arrows indicate rapid cooling phases (see Section 4.2 for details). For the entire time-temperature space of the thermal models shown here, all thermal models conducted, and detailed information, see Figs. S2 and S3, and Table S6.

Rocks exposed on the interfluves show deeper exhumation than plateau rocks, while the onset of exhumation appears similar at $\sim\!40\text{--}35$ Ma (18PE04, Fig. 7b; ZHe (single-grain) ages at $>\!4000$ m, Fig. 5c). Following this, faster exhumation occurred either continuously from $\sim\!22$ Ma to $\sim\!8$ Ma or in two phases at $\sim\!22\text{--}15$ Ma and $\sim\!12\text{--}8$ Ma.

Rocks exposed in canyon bottoms suggest exhumation initiated ~ 35 Ma with phases of acceleration at ~ 25 –15 Ma, ~ 10 –8 Ma (or ~ 8 Ma), and one or two episodes since ~ 5 Ma. The most notable along-strike difference in canyon exhumation is the magnitude. The exhumation magnitude since 5 Ma was 2.9–5.6 km for the San Gabán Canyon and 4.4–8.3 km for the Marcapata Canyon. These ranges in exhumation magnitude estimates assume exhumation from depth with temperatures of $100\,^{\circ}\text{C}$ (San Gabán,

Fig. 8a) and, on average, 150 °C (Marcapata, Fig. 8b), and a paleogeothermal gradient of 26±8 °C/km for the Eastern Cordillera (following Barnes et al., 2008). The estimates are simplified and do not account for advection and topographic effects, but the difference in exhumation magnitude is a robust result. The higher exhumation magnitude (compared to the San Gabán Canyon) and good sample coverage of the Marcapata Canvon (compared to the Tres Cruces Canvon) favor a better resolution of the thermal history. which suggests there may have been two distinct cooling phases. one \sim 6-3 Ma and one since \sim 2-1 Ma (Figs. 5d, 8b). The youngest resolved rapid exhumation phase of the San Gabán Canyon bottom occurred at \sim 4 Ma (Figs. 3b, 8a). The exhumation history of the Tres Cruces Canyon might have been similar to the Marcapata Canyon with an exhumation phase around 8 Ma and since \sim 4–3 Ma (thermal histories, Fig. 8c) or possibly 5-4 Ma (AHe ages of higher-elevation samples, Fig. 6, Section 4.1.3), but this result is not well constrained.

Finally, the latest exhumation onset time was in the Subandes. The prevalence of <10 Ma AHe single-grain ages in partially reset samples suggests that exhumation was ongoing by $\sim\!10$ Ma (Tables 2, S1). Perez et al. (2016a) suggested Subandean exhumation initiated after $\sim\!15$ Ma and by $\sim\!6$ Ma in the study area. This timing is similar to observations of a 19–14 Ma, or 13–10 Ma start of exhumation in northern Bolivia (Rak et al., 2017; Buford Parks and McQuarrie, 2019) and a $\sim\!14$ Ma start northwest of the Abancay Deflection (Espurt et al., 2011).

5.2. Tectonic and structural signals of exhumation

Previous studies interpreted an onset of Eastern Cordilleran deformation between 55 and 40 Ma in northern Bolivia and southeasternmost Peru (e.g., Farrar et al., 1988; Kontak et al., 1990; Perez and Levine, 2020). In the region investigated here, evidence for erosional exhumation and, by association, active deformation is suggested by $\sim\!40$ Ma (and possibly earlier). Furthermore, we find Miocene (and younger) phases of accelerated exhumation as described above (Section 5.1).

The first-order pattern of thermochronometric ages in the study area resembles what is expected from the thermal evolution of a deforming crustal wedge and the emplacement of basement thrust sheets over time. A "U-shape" pattern in thermochronometric ages, as seen in the northeastern Peruvian Eastern Cordillera (Figs. 2b, 5b, 6b) and other orogens (e.g., McQuarrie and Ehlers, 2015; Rak et al., 2017; Buford Parks and McQuarrie, 2019; Andrić-Tomašević et al., 2021; Eizenhöfer et al., 2021, 2023), is typically a function of the movement of rocks over ramps, resulting in rock uplift, increased elevation and relief, and consequently enhanced erosional exhumation. After vertical motion along a ramp, rocks that cooled through thermochronometer closure temperatures are moved laterally along structural flats (Huerta and Rodgers, 2006; Lock and Willett, 2008; McQuarrie and Ehlers, 2015, 2017; Rak et al., 2017). For the San Gabán balanced cross-section, Perez et al. (2016a) suggested the presence of a 10-km-high ramp beneath the northeastern Eastern Cordillera, which could produce the observed general age pattern with young ages above and northeast of the ramp, and older and partially and unreset ages toward the frontal part of the Eastern Cordillera and Subandes and in the Macusani Structural Zone (Figs. 2b, 2c). However, the extent of uplift over an active ramp suggested by the cross-section (\sim 20–25 km, Fig. 2c) is much narrower than the regions of documented incision, as indicated by the narrow age range of the wide, flat part of the "U-shape" age trends over at least 50 km independent of elevation (Figs. 2, 5, Section 4.1). This suggests that exhumation driven by crustal shortening alone cannot produce the details of the thermochronometric age pattern in the canyons (Section 5.3).

In contrast to the northeastern Eastern Cordillera described above, the first-order thermochronometric age trend of the backthrust belt (younging toward the Ayaviri fault system, Fig. 2b) might be inexplicable with the previously suggested basement structures of Perez et al. (2016a). The main activity of the Ayaviri Fault occurred in the late Oligocene (Perez and Horton, 2014) and cannot explain the Miocene (and even Pliocene on the other transects; Figs. 5b, 6b) AHe ages in its proximity or the overall age trend of the backthrust belt. Another southwest-dipping basement ramp beneath the Altiplano-Eastern Cordillera border area could produce the observed age trend, similar to the suggested structural solution and age trend (although older ages) of the backthrust belt in northern Bolivia (McQuarrie et al., 2008; Rak et al., 2017). In contrast, the younger (Pliocene) AHe ages of the northwestern two transects' backthrust belt region might be related to the rivers that incise the plateau from the northwest (since ~4 Ma, Gérard et al., 2021a) and have their headwaters in the northwestern backthrust belt (Cusco and Sicuani areas, Fig. 1). Alternatively, Gérard et al. (2021b) suggested interactions between climate-driven incision and Pliocene Ayaviri Fault reactivation in the Abancay Deflection

Due to the similarity between the three transects' thermochronometric age patterns (Sections 4.1, 5.1), we suggest the structural architectures and kinematic histories should also be similar. However, some differences must exist given the higher-magnitude exhumation and potential differences in <10 Ma cooling histories of the northeastern portions of the Marcapata and Tres Cruces transects. As the observed thermochronometric ages likely reflect, to a large part, an integrated signal of structural deformation over time, flexural kinematic modeling can help to explore, among other things, possible differences in structural solutions of the study area (see Buford Parks et al., 2023; Glover et al., 2023).

5.3. Evaluating Pliocene-Present regional incision

This study was motivated by the need for constraints on the temporal and spatial pattern of canyon incision in the context of the region's long-term deformation and exhumation histories. Results from this study and other recent thermochronologic observations from canyon bottom samples confirm that plateau incision did occur regionally, at least from the Abancay Deflection to southern Bolivia (Fig. 1 inset map). In addition, exhumation in canyons accelerated synchronously at \sim 4–3 Ma (or more precisely at \sim 4 Ma (Abancay Deflection; Gérard et al., 2021a), between ∼6 and \sim 3 Ma (Marcapata and Tres Cruces), at \sim 4 Ma (San Gabán; Lease and Ehlers, 2013; this study), and ~3 Ma in southern and northern Bolivia (Kennan et al., 1997; Zeilinger and Schlunegger, 2007; McQuarrie et al., 2008)). Furthermore, new results from the Marcapata Canyon indicate a possible second episode of incision at or since 2-1 Ma. Whether this two-phase incision is unique to the Marcapata Canyon or continuous along strike requires further investigation.

It is beyond the temporal resolution of our data (see Sections 4.2.3, 5.1) to more precisely assess how much natural variability exists in the onset of Pliocene incision. However, it is conceivable that, independent of the driver of incision, the timing of incision varies slightly along-strike given the variability in lithologies exposed, and local variations in the structural architecture. Both of these factors could affect the long-term exhumation upon which the incision signal is superimposed (Section 5.2). In contrast to the previous interpretation of Pliocene canyon incision in the absence of post-mid Miocene deformation (Lease and Ehlers, 2013), the new data presented here suggest a more complicated picture. Our results document regional deformation-driven exhumation continued during the Miocene (and potentially to the Present) and was augmented with a regional incision-related ex-

humation signal that initiated in the last \sim 4 Myrs. The time window of ramp uplift is much longer (\sim 15 Myrs, as indicated by AHe ages on the interfluves, the old side of the "U-shape" age pattern) than the time window of the incision. This means that a more recent (Pliocene) ramp uplift, which was an alternative explanation for canyon incision (Whipple and Gasparini, 2014), would likely not produce the observed thermochronometric ages of canyons and interfluves.

While we cannot directly determine the drivers of Pliocene plateau incision from our data, we suggest that in addition to continuous structural uplift, as described above, Pliocene paleoclimate change resulted in rapid canyon incision. A detailed review of Pliocene (and older) South American paleoclimate change is beyond the scope of this study. However, we note that recent studies support the earlier interpretation of Lease and Ehlers (2013) that the Pliocene to recent climate change enhanced moisture transport to the eastern flank of the Central Andes. More specifically, Mutz et al. (2018) and Mutz and Ehlers (2019) presented a series of global paleoclimate model timeslice (Pliocene-Present) experiments. They found that Pliocene to recent precipitation along the eastern flank of the Central Andes has increased by having more consecutive wet days and higher maximum precipitation rates. Going to earlier than the Pliocene, the climatology of the region is less well known. What is clear from existing paleoclimate modeling studies (e.g., Ehlers and Poulsen, 2009; Poulsen et al., 2010; Jeffery et al., 2012) is that the Eocene to Present rise of the Andean Plateau led to regional climate change and progressively wetter conditions along the eastern flank of the Central Andes.

The previous changes in paleo to modern precipitation could have resulted in regional, synchronous enhanced erosion and incision across regions with different deformation histories. Previous studies have shown the potential for significant changes in river incision due to changing climate (Ferrier et al., 2013; Jeffery et al., 2013). However, just as structurally driven erosion cannot explain all the observed canyon incision, paleoclimate change-driven erosion alone also cannot. This is indicated by the continuous, postmid Miocene exhumation signal that we interpret as deformationrelated, and, importantly, the exhumation magnitude (at least in the Marcapata region, and likely in the other regions of the study area as well) that exceeds the 2.5-3 km depth of canyons. To quantify the deformation history and effects of deformation, uplift, and incision on the observed thermochronometer data, flexural kinematic and thermo-kinematic modeling of geologic cross-sections can be used (see Buford Parks et al., 2023, and Glover et al., 2023). A process-based modeling test of the effect of paleoclimate change on eastern Andean Plateau fluvial incision is however beyond the scope of these studies, and awaits future investigation.

6. Conclusions

We presented new multi-thermochronometer data from 51 new and eight previous bedrock samples, combined with previous thermochronometer data from 15 bedrock samples, from three transects across the eastern Central Andes in southern Peru. The data suggest a northeastward progression of deformation-related exhumation from an onset in the late Eocene (plateau) to the early to mid-Miocene (Subandes). While the overall trends in thermochronometric ages are similar for all three sections, the exhumation magnitude differs, suggesting some differences in the structural architecture in southern Peru over <200 km distance.

At today's plateau flank, the deformation-related exhumation is superimposed with a regional, synchronous incision-related exhumation signal since the Pliocene. While active basement structures have been proposed along the regionally extensive (over 1,250 km) plateau edge where \sim 4–3 Ma incision is recognized, the time window of ramp uplift is much longer (\sim 15 Myrs) than

the age of incision and the location of active uplift (20–25 km) is notably narrower than the >50 km regions of documented incision. We suggest that paleoclimate change contributed significantly to canyon incision, based on its regional extent and synchronicity across areas of different deformation histories and exhumation magnitudes. However, the observations of continuing post mid-Miocene deformation-related exhumation and the high exhumation magnitude support contributions from both paleoclimate change and tectonics for the present-day topography.

Observations of the spatio-temporal patterns of canyon incision need to be placed into the context of the long-term regional deformation and exhumation history to evaluate possible tectonic vs. paleoclimate change mechanisms. Specifically, thermochronometer samples from just canyon bottoms would not be sufficient to reveal a complex story with superimposing exhumation signals from different drivers. In general, disentangling impacts of paleoclimate and tectonic change requires a broader sampling strategy, and the integration between diverse methods such as geoand thermochronology, structural geology, flexural kinematic reconstructions, landscape analyses, and paleoclimate modeling.

CRediT authorship contribution statement

Sarah Falkowski: Conceptualization, Data curation, Formal analysis, Funding acquisition, Investigation, Methodology, Project administration, Visualization, Writing – original draft. **Todd A. Ehlers:** Conceptualization, Resources, Supervision, Validation, Writing – review & editing. **Nadine McQuarrie:** Conceptualization, Funding acquisition, Investigation, Validation, Writing – review & editing. **Chloë O. Glover:** Investigation, Writing – review & editing. **Nicholas D. Perez:** Writing – review & editing. **Victoria M. Buford Parks:** Funding acquisition, Investigation, Writing – review & editing.

Declaration of competing interest

The authors declare that they have no known competing financial interests or personal relationships that could have appeared to influence the work reported in this paper.

Data availability

All previously published data used in this study are available through publications referenced. All new data (presented in Tables S1–S5) are archived through PANGAEA (Falkowski, S., and Ehlers, T.A., 2023, https://doi.pangaea.de/10.1594/PANGAEA.955437).

Acknowledgements

This work was supported by the DFG (German Research Foundation, grant FA 1489/1-1 to S.F.), NSF (National Science Foundation, grant EAR-1842172 to N.M.), and NASA headquarters (NASA Earth and Space Science Fellowship program, grant 80NSSC17K0388 to V.B.P.). We thank the Gil family for logistical support during fieldwork. Christoph Glotzbach supported isotope dilution ICP-MS measurements at the University of Tübingen. Jason Barnes collected three of the presented samples (06JBPR10, 06JBPR17, 06JBPR19). Richard Lease picked these three samples for AHe measurements.

We thank Alex Webb for editorial handling. The comments and suggestions of two reviewers helped us to clarify the manuscript.

Appendix A. Supplementary material

Supplementary material related to this article can be found online at https://doi.org/10.1016/j.epsl.2023.118299.

References

- Allmendinger, R.W., Jordan, T.E., Kay, S.M., Isacks, B.L., 1997. The evolution of the Altiplano-Puna plateau of the Central Andes. Annu. Rev. Earth Planet. Sci. 25, 139–174. https://doi.org/10.1146/annurev.earth.25.1.139.
- Andrić-Tomašević, N., Falkowski, S., Georgieva, V., Glotzbach, C., Strecker, M.R., Ehlers, T.A., 2021. Quantifying tectonic and glacial controls on topography in the Patagonian Andes (46.5°S) from integrated thermochronometry and thermokinematic modeling. J. Geophys. Res., Earth Surf. 126. https://doi.org/10.1029/2020if005993.
- Baby, P., Calderón, Y., Hurtado, C., Louterbach, M., Espurt, N., Brusset, S., Roddaz, M., Brichau, S., Eude, A., Calves, G., Quispe, A., Ramirez, L., Bandach, A., Bolaños, R., 2018. The Peruvian sub-Andean foreland basin system: structural overview, geochronologic constraints, and unexplored plays. In: Zamora, G., McClay, K.R., Ramos, V.A. (Eds.), Petroleum Basins and Hydrocarbon Potential of the Andes of Peru and Bolivia. In: AAPG Memoir. The American Association of Petroleum Geologists, pp. 87–116.
- Barnes, J.B., Ehlers, T.A., McQuarrie, N., O'Sullivan, P.B., Tawackoli, S., 2008. Thermochronometer record of central Andean Plateau growth, Bolivia (19.5°S). Tectonics 27. https://doi.org/10.1029/2007TC002174.
- Bookhagen, B., Strecker, M.R., 2012. Spatiotemporal trends in erosion rates across a pronounced rainfall gradient: examples from the southern Central Andes. Earth Planet. Sci. Lett. 327–328, 97–110. https://doi.org/10.1016/j.epsl.2012.02.005.
- Buford Parks, V.M., McQuarrie, N., 2019. Kinematic, flexural, and thermal modelling in the Central Andes: unravelling age and signal of deformation, exhumation, and uplift. Tectonophysics 766, 302–325. https://doi.org/10.1016/j.tecto.2019.06. 008.
- Buford Parks, V.M., McQuarrie, N., Falkowski, S., Perez, N.D., Ehlers, T.A., 2023. Timing and drivers of exhumation and sedimentation in the eastern Peruvian Andes: insights from thermokinematic modelling. Earth Planet. Sci. Lett. 620, 118355. https://doi.org/10.1016/j.epsl.2023.118355.
- Brandon, M.T., Roden-Tice, M.K., Garver, J.I., 1998. Late Cenozoic exhumation of the Cascadia accretionary wedge in the Olympic Mountains, northwest Washington State. Geol. Soc. Am. Bull. 110, 985–1009. https://doi.org/10.1130/0016-7606(1998)110<0985:LCEOTC>2.3.CO:2.
- Carlotto, V., 2013. Paleogeographic and tectonic controls on the evolution of Cenozoic basins in the Altiplano and Western Cordillera of southern Peru. Tectonophysics 589, 195–219. https://doi.org/10.1016/j.tecto.2013.01.002.
- Donelick, R.A., 2005. Apatite fission-track analysis. Rev. Mineral. Geochem. 58, 49–94. https://doi.org/10.2138/rmg.2005.58.3.
- Ehlers, T.A., Poulsen, C.J., 2009. Influence of Andean uplift on climate and paleoal-timetry estimates. Earth Planet. Sci. Lett. 281, 238–248. https://doi.org/10.1016/j.epsl.2009.02.026.
- Eizenhöfer, P.R., Glotzbach, C., Büttner, L., Kley, J., Ehlers, T.A., 2021. Turning the orogenic switch: slab-reversal in the Eastern Alps recorded by lowtemperature thermochronology. Geophys. Res. Lett. 48, 17. https://doi.org/10. 1029/2020GL092121.
- Eizenhöfer, P.R., Glotzbach, C., Kley, J., Ehlers, T.A., 2023. Thermo-kinematic evolution of the Eastern European Alps along the TRANSALP transect. Tectonics 42, e2022TC007380. https://doi.org/10.1029/2022TC007380.
- Espurt, N., Barbarand, J., Roddaz, M., Brusset, S., Baby, P., Saillard, M., Hermoza, W., 2011. A scenario for late Neogene Andean shortening transfer in the Camisea Subandean zone (Peru, 12°S): implications for growth of the northern Andean Plateau. Geol. Soc. Am. Bull. 123, 2050–2068. https://doi.org/10.1130/b30165.1.
- Eude, A., Roddaz, M., Brichau, S., Brusset, S., Calderon, Y., Baby, P., Soula, J.-C., 2015. Controls on timing of exhumation and deformation in the northern Peruvian eastern Andean wedge as inferred from low-temperature thermochronology and balanced cross section. Tectonics 34, 715–730. https://doi.org/10.1002/ 2014TC003641.
- Falkowski, S., Ehlers, T.A., 2023. Low-temperature thermochronometric data (AHe, AFT, ZHe, ZFT) from three bedrock sample transects across the eastern Central Andes, southern Peru. PANGAEA. https://doi.pangaea.de/10.1594/PANGAEA. 955437.
- Farley, K.A., 2000. Helium diffusion from apatite: general behavior as illustrated by Durango fluorapatite. J. Geophys. Res., Solid Earth 105, 2903–2914. https://doi.org/10.1029/1999JB900348.
- Farrar, E., Clark, A.H., Kontak, D.J., Archibald, D.A., 1988. Zongo-San Gabán zone: Eocene foreland boundary of the Central Andean orogen, northwest Bolivia and southeast Peru. Geology 16, 55. https://doi.org/10.1130/0091-7613(1988) 016<0055:ZSGNZE>2.3.CO;2.
- Ferrier, K.L., Huppert, K.L., Perron, J.T., 2013. Climatic control of bedrock river incision. Nature 496, 206–209. https://doi.org/10.1038/nature11982.
- Gallagher, K., 2012. Transdimensional inverse thermal history modeling for quantitative thermochronology. J. Geophys. Res., Solid Earth 117. https://doi.org/10.1029/2011JB008825.
- Garver, J.I., 2003. Etching zircon age standards for fission-track analysis. Radiat. Meas. 37, 47–53. https://doi.org/10.1016/S1350-4487(02)00127-0.
- Gasparini, N.M., Whipple, K.X., 2014. Diagnosing climatic and tectonic controls on topography: eastern flank of the northern Bolivian Andes. Lithosphere 6, 230–250. https://doi.org/10.1130/L322.1.

- Gérard, B., Audin, L., Robert, X., Gautheron, C., van der Beek, P., Bernet, M., Benavente, C., Delgado, F., 2021a. Pliocene river capture and incision of the northern Altiplano: Machu Picchu, Peru. J. Geol. Soc. 178, 11. https://doi.org/10.1144/jgs2020-100.
- Gérard, B., Robert, X., Audin, L., Valla, P.G., Bernet, M., Gautheron, C., 2021b. Differential exhumation of the Eastern Cordillera in the Central Andes: evidence for south-verging backthrusting (Abancay deflection, Peru). Tectonics 40. https://doi.org/10.1029/2020TC006314.
- Glotzbach, C., Lang, K.A., Avdievitch, N.N., Ehlers, T.A., 2019. Increasing the accuracy of (U-Th(-Sm))/He dating with 3D grain modelling. Chem. Geol. 506, 113–125. https://doi.org/10.1016/j.chemgeo.2018.12.032.
- Glotzbach, C., van der Beek, P.A., Spiegel, C., 2011. Episodic exhumation and relief growth in the Mont Blanc massif, Western Alps from numerical modelling of thermochronology data. Earth Planet. Sci. Lett. 304, 417–430. https://doi.org/10. 1016/j.epsl.2011.02.020.
- Glover, C.O., McQuarrie, N., Falkowski, S., Ehlers, T.A., 2023. Assessing drivers of high exhumation magnitudes and young cooling ages in the eastern Central Andes, southern Peru (13–18°S). Earth Planet. Sci. Lett. 620, 118281. https://doi.org/10.1016/j.epsl.2023.118281.
- Godard, V., Bourles, D.L., Spinabella, F., Burbank, D.W., Bookhagen, B., Fisher, G.B., Moulin, A., Leanni, L., 2014. Dominance of tectonics over climate in Himalayan denudation. Geology 42, 243–246. https://doi.org/10.1130/G35342.1.
- Gotberg, N., McQuarrie, N., Caillaux, V.C., 2010. Comparison of crustal thickening budget and shortening estimates in southern Peru (12-14°S): implications for mass balance and rotations in the "Bolivian orocline.". Geol. Soc. Am. Bull. 122, 727–742. https://doi.org/10.1130/B26477.1.
- Harrison, T.M., Duncan, I., McDougall, I., 1985. Diffusion of 40Ar in biotite: temperature, pressure and compositional effects. Geochim. Cosmochim. Acta 49, 2461–2468. https://doi.org/10.1016/0016-7037(85)90246-7.
- Horton, B.K., Hampton, B.A., Lareau, B.N., Baldellon, E., 2002. Tertiary provenance history of the Northern and Central Altiplano (Central Andes, Bolivia): a detrital record of Plateau-Margin Tectonics. J. Sediment. Res. 72, 711–726. https://doi. org/10.1306/020702720711.
- Huerta, A.D., Rodgers, D.W., 2006. Constraining rates of thrusting and erosion: insights from kinematic thermal modeling. Geology 34, 541–544. https://doi.org/10.1130/G22421.1.
- Hurford, A.J., 1990. Standardization of fission track dating calibration: recommendation by the fission track working group of the I.U.G.S. subcommission on geochronology. Chem. Geol. 80, 171–178.
- INGEMMET, 2022. Geological Map of Peru (1:1,000,000). Instituto Geológico Minero y Metalúrgico (INGEMMET), Lima, Peru. https://hdl.handle.net/20.500.12544/3859
- Isacks, B.L., 1988. Uplift of the Central Andean Plateau and bending of the Bolivian Orocline. J. Geophys. Res. 93, 3211. https://doi.org/10.1029/JB093iB04p03211.
- Jeffery, M.L., Poulsen, C.J., Ehlers, T.A., 2012. Impacts of Cenozoic global cooling, surface uplift, and an inland seaway on South American paleoclimate and precipitation 18O. Geol. Soc. Am. Bull. 124, 335–351. https://doi.org/10.1130/B30480.1.
- Jeffery, M.L., Ehlers, T.A., Yanites, B.J., Poulsen, C.J., 2013. Quantifying the role of paleoclimate and Andean Plateau uplift on river incision. J. Geophys. Res., Earth Surf. 118, 852–871. https://doi.org/10.1002/jgrf.20055.
- Kennan, L., Lamb, S.H., Hoke, L., 1997. High-altitude palaeosurfaces in the Bolivian Andes: evidence for late Cenozoic surface uplift. Geol. Soc. (Lond.) Spec. Publ. 120, 307–323. https://doi.org/10.1144/gsl.sp.1997.120.01.20.
- Ketcham, R.A., Carter, A., Donelick, R.A., Barbarand, J., Hurford, A.J., 2007. Improved modeling of fission-track annealing in apatite. Am. Mineral. 92, 799–810. https://doi.org/10.2138/am.2007.2281.
- Kirby, E., Whipple, K.X., Tang, W., Chen, Z., 2003. Distribution of active rock uplift along the eastern margin of the Tibetan Plateau: inferences from bedrock channel longitudinal profiles. J. Geophys. Res., Solid Earth 108. https://doi.org/10.1029/2001/B000861.
- Kontak, D.J., Farrar, E., Clark, A.H., Archibald, D.A., 1990. Eocene tectono-thermal rejuvenation of an upper Paleozoic-lower Mesozoic terrane in the Cordillera de Carabaya, Puno, southeastern Peru, revealed by K-Ar and 40Ar/39Ar dating. J. South Am. Earth Sci. 3, 231–246. https://doi.org/10.1016/0895-9811(90)90005-L.
- Lamb, S., Davis, P., 2003. Cenozoic climate change as a possible cause for the rise of the Andes. Nature 425, 792–797. https://doi.org/10.1038/nature02049.
- Lancelot, J.R., Laubacher, G., Marocco, R., Renaud, U., 1978. U/Pb radiochronology of two granitic plutons from the Eastern Cordillera (Peru) – extent of permian magmatic activity and consequences. Geol. Rundsch. 67, 236–243. https://doi. org/10.1007/bf01803263.
- Lease, R.O., Ehlers, T.A., 2013. Incision into the Eastern Andean Plateau during Pliocene cooling. Science 341, 774–776. https://doi.org/10.1126/science.1239132.
- Lock, J., Willett, S., 2008. Low-temperature thermochronometric ages in fold-and-thrust belts. Tectonophysics 456, 147–162. https://doi.org/10.1016/j.tecto.2008.03.007.
- McQuarrie, N., Barnes, J.B., Ehlers, T.A., 2008. Geometric, kinematic, and erosional history of the central Andean Plateau, Bolivia (15–17°S). Tectonics 27, TC3007. https://doi.org/10.1029/2006TC002054.
- McQuarrie, N., DeCelles, P., 2001. Geometry and structural evolution of the central Andean backthrust belt, Bolivia. Tectonics 20, 669–692. https://doi.org/10.1029/2000TC001232.

- McQuarrie, N., Ehlers, T.A., 2017. Techniques for understanding fold-and-thrust belt kinematics and thermal evolution. In: Law, R.D., Thigpen, J.R., Merschat, A.J., Stowell, H.H. (Eds.), Linkages and Feedbacks in Orogenic Systems, Geological Society of America Memoir. Geological Society of America, pp. 1–30.
- McQuarrie, N., Ehlers, T.A., 2015. Influence of thrust belt geometry and shortening rate on thermochronometer cooling ages: insights from thermochrometic and erosion modeling of the Bhutan Himalaya. Tectonics 34, 1055–1079. https://doi.org/10.1002/2014TC003783.
- Mišković, A., Spikings, R.A., Chew, D.M., Košler, J., Ulianov, A., Schaltegger, U., 2009. Tectonomagmatic evolution of Western Amazonia: geochemical characterization and zircon U-Pb geochronologic constraints from the Peruvian Eastern Cordilleran granitoids. Geol. Soc. Am. Bull. 121, 1298–1324. https://doi.org/10.1130/R76488.1
- Montgomery, D.R., Balco, G., Willett, S.D., 2001. Climate, tectonics, and the morphology of the Andes. Geology 29, 579–582. https://doi.org/10.1130/0091-7613(2001)029<0579:CTATMO>2.0.CO;2.
- Mutz, S.G., Ehlers, T.A., 2019. Detection and explanation of spatiotemporal patterns in Late Cenozoic palaeoclimate change relevant to Earth surface processes. Earth Surf. Dyn. 7, 663–679. https://doi.org/10.5194/esurf-7-663-2019.
- Mutz, S.G., Ehlers, T.A., Werner, M., Lohmann, G., Stepanek, C., Li, J., 2018. Estimates of late Cenozoic climate change relevant to Earth surface processes in tectonically active orogens. Earth Surf. Dyn. 6, 271–301. https://doi.org/10.5194/esurf-6-271-2018
- Perez, N.D., Horton, B.K., 2014. Oligocene-Miocene deformational and depositional history of the Andean hinterland basin in the northern Altiplano plateau, southern Peru. Tectonics 33, 1819–1847. https://doi.org/10.1002/2014TC003647.
- Perez, N.D., Horton, B.K., McQuarrie, N., Stübner, K., Ehlers, T.A., 2016a. Andean shortening, inversion and exhumation associated with thin- and thick-skinned deformation in southern Peru. Geol. Mag. 153, 1013–1041. https://doi.org/10. 1017/S0016756816000121.
- Perez, N.D., Horton, B.K., Carlotto, V., 2016b. Structural inheritance and selective reactivation in the central Andes: Cenozoic deformation guided by pre-Andean structures in southern Peru. Tectonophysics 671, 264–280. https://doi.org/10.1016/j.tecto.2015.12.031.

- Perez, N.D., Levine, K.G., 2020. Diagnosing an ancient shallow-angle subduction event from Cenozoic depositional and deformational records in the central Andes of southern Peru. Earth Planet. Sci. Lett. 541, 116263. https://doi.org/10.1016/j.epsl.2020.116263.
- Poulsen, C.J., Ehlers, T.A., Insel, N., 2010. Onset of convective rainfall during gradual late miocene rise of the Central Andes. Science 328, 490–493. https://doi.org/10.1126/science.1185078.
- Rak, A.J., McQuarrie, N., Ehlers, T.A., 2017. Kinematics, exhumation, and sedimentation of the North Central Andes (Bolivia): an integrated thermochronometer and thermokinematic modeling approach. Tectonics 36, 2524–2554. https://doi.org/10.1002/2016TC004440.
- Reiners, P.W., 2005. Zircon (U-Th)/He thermochronometry. Rev. Mineral. Geochem. 58, 151–179. https://doi.org/10.2138/rmg.2005.58.6.
- Reiners, P.W., Spell, T.L., Nicolescu, S., Zanetti, K.A., 2004. Zircon (U-Th)/He thermochronometry: He diffusion and comparisons with 40Ar/39Ar dating. Geochim. Cosmochim. Acta 68, 1857–1887. https://doi.org/10.1016/j.gca.2003. 10.021.
- Ruiz, G.M.H., Carlotto, V., Van Heiningen, P.V., Andriessen, P.A.M., 2009. Steady-state exhumation pattern in the Central Andes - SE Peru. Geol. Soc. (Lond.) Spec. Publ. 324, 307–316. https://doi.org/10.1144/SP324.20.
- Stübner, K., Drost, K., Schoenberg, R., Böhme, M., Starke, J., Ehlers, T.A., 2016. Asynchronous timing of extension and basin formation in the South Rhodope core complex, SW Bulgaria, and northern Greece. Tectonics 35, 136–159. https://doi.org/10.1002/2015TC004044.
- Whipple, K.X., Gasparini, N.M., 2014. Tectonic control of topography, rainfall patterns, and erosion during rapid post–12 Ma uplift of the Bolivian Andes. Lithosphere 6, 251–268. https://doi.org/10.1130/l325.1.
- Zeilinger, G., Schlunegger, F., 2007. Possible flexural accommodation on the eastern edge of the Altiplano in relation to focussed erosion in the Rio La Paz drainage system. Terra Nova 19, 373–380. https://doi.org/10.1111/j.1365-3121.